2016

PROBING PHYSICAL CONDITIONS IN THE CRAB NEBULA WITH EMISSION LINE ANALYSIS

Xiang Wang
University of Kentucky, xiangwang713@gmail.com
Digital Object Identifier: http://dx.doi.org/10.13023/ETD.2016.109

STUDENT AGREEMENT:

I represent that my thesis or dissertation and abstract are my original work. Proper attribution has been given to all outside sources. I understand that I am solely responsible for obtaining any needed copyright permissions. I have obtained needed written permission statement(s) from the owner(s) of each third-party copyrighted matter to be included in my work, allowing electronic distribution (if such use is not permitted by the fair use doctrine) which will be submitted to UKnowledge as Additional File.

I hereby grant to The University of Kentucky and its agents the irrevocable, non-exclusive, and royalty-free license to archive and make accessible my work in whole or in part in all forms of media, now or hereafter known. I agree that the document mentioned above may be made available immediately for worldwide access unless an embargo applies.

I retain all other ownership rights to the copyright of my work. I also retain the right to use in future works (such as articles or books) all or part of my work. I understand that I am free to register the copyright to my work.

REVIEW, APPROVAL AND ACCEPTANCE

The document mentioned above has been reviewed and accepted by the student's advisor, on behalf of the advisory committee, and by the Director of Graduate Studies (DGS), on behalf of the program; we verify that this is the final, approved version of the student's thesis including all changes required by the advisory committee. The undersigned agree to abide by the statements above.

Xiang Wang, Student

Dr. Gary J. Ferland, Major Professor

Dr. Tim Gorringe, Director of Graduate Studies

PROBING PHYSICAL CONDITIONS IN THE CRAB NEBULA WITH EMISSION LINE ANALYSIS

DISSERTATION

A thesis submitted in partial fulfillment of the
requirements for the degree of Doctor of Philosophy in the
College of Arts and Sciences
at the University of Kentucky

By

Xiang Wang

Lexington, Kentucky

Director: Dr. Gary Ferland, Professor of Physics

Lexington, Kentucky

2016

ABSTRACT OF DISSERTATION

PROBING PHYSICAL CONDITIONS IN THE CRAB NEBULA
WITH EMISSION LINE ANALYSIS

We present a range of steady-state photoionization simulations, corresponding to different assumed shell geometries and compositions, of the unseen postulated rapidly expanding outer shell to the Crab Nebula. The properties of the shell are constrained by the mass that must lie within it, and by limits to the intensities of hydrogen recombination lines. In all cases the photoionization models predict very strong emission from high ionization lines that will not be emitted by the Crab's filaments, alleviating problems with detecting these lines in the presence of light scattered from brighter parts of the Crab. The NIR [Ne VI] $\lambda 7.652$ μm line is a particularly good case; it should be dramatically brighter than the optical lines commonly used in searches. The C IV $\lambda 1549$Å doublet is predicted to be the strongest absorption line from the shell, which is in agreement with HST observations. We show that the cooling timescale for the outer shell is much longer than the age of the Crab, due to the low density. This means that the temperature of the shell will actually "remember" its initial conditions. However, the recombination time is much shorter than the age of the Crab, so the predicted level of ionization should approximate the real ionization. In any case, it is clear that IR observations present the best opportunity to detect the outer shell and so guide future models that will constrain early events in the original explosion.

Infrared observations have discovered a variety of objects, including filaments in the Crab Nebula and cool-core clusters of galaxies, where the H_2 1-0 S(1) line is stronger than the infrared H I lines. A variety of processes could be responsible for this emission. Although many complete shock or PDR calculations of H_2 emission have been published, we know of no previous simple calculation that shows the emission spectrum and level populations of thermally excited low-density H_2. We present a range of purely thermal collisional simulations, corresponding to constant gas kinetic temperature at different densities. We consider the cases where the collisions affecting H_2 are predominantly with atomic or molecular hydrogen. The resulting level population (often called "excitation") diagrams show that excitation temperatures are sometimes lower than the gas kinetic temperature when the density is too low for the level populations to go to LTE. The atomic case goes to LTE at much lower densities than the molecular case due to larger collision rates. At low densities for the *v*=1 and 2 vibrational manifolds level populations are quasi-

thermal, which could be misinterpreted as showing the gas is in LTE at high density. At low densities for the molecular case the level population diagrams are discontinuous between v=0 and 1 vibrational manifolds and between v=2, J=0, 1 and other higher J levels within the same vibrational manifold. These jumps could be used as density diagnostics. We show how much the H_2 mass would be underestimated using the H_2 1-0 S(1) line strength if the density is below that required for LTE. We give diagnostic diagrams showing level populations over a range of density and temperature. The density where the level populations are given by a Boltzmann distribution relative to the total molecular abundance (required to get the correct H_2 mass), is shown for various cases. We discuss the implications of these results for the interpretation of H_2 observations of the Crab Nebula and filaments in cool-core clusters of galaxies.

Key words: supernova remnants, Crab Nebula, interstellar medium, Abell 2597, molecular hydrogen, CLOUDY

Author's Signature: Xiang Wang

Date: February 17, 2016

PROBING PHYSICAL CONDITIONS IN THE CRAB NEBULA WITH EMISSION ANALYSIS

By

Xiang Wang

Gary Ferland
Director of Thesis

Tim Gorringe
Director of Graduate Studies

February 17, 2016
Date

To my family…

ACKNOWLEDGMENTS

I would like to express my greatest appreciation to my advisor, Dr. Gary Ferland for his guidance, encouragement and support in my study and research in the past five years. I would never have been able to finish my dissertation without his inspiration, insight into problems and intelligent guidance.

I would like to thank the other members of my advisory committee, Dr. Ron Wilhelm, Dr. Renbin Yan and Dr. Steven Yates for their time and guidance.

I wish to express my sincere gratitude to the co-authors of my publications, Dr. Jack Baldwin and Dr. Edwin Loh from Michigan State University, Dr. Andy Fabian from Cambridge University, as well as Dr. Robin Williams from AWE.

I also would like to thank professors who deeply helped me in my course study in the department of physics and astronomy, Dr. Sumit Das, Dr. Michael Eides, Dr. Ribhu Kaul, Dr. Bingan Li, and Dr. Isaac Shlosman.

I will never forget all the help and supports from my colleagues and friends Hao Zhang, Ye Wang, Kai Zhang, Yulong Yao, Jin Xu, Gen Wang, Shaoqian Wang, Hongwei Yang, Mingyang Sun, Filmon Misgina, Mirza Islam, Marios Chatzikos, Francisco Guzman, Jiao Lei, Gang Yu, and Caibo Hu. Without these friends, it would have been very difficult to spend more than five years at Lexington, a city so far from my hometown.

Finally, I am very grateful to all my family. I would like to express my special appreciation and love to my wife Shengxi He who always supports me with deepest love and blessing, my father Chuanqing Wang who always encourages me from China, my late mother Li Su who firstly inspired me to study abroad, and my mother-in-law Mei Dai who helps take care of my daughter Stella.

List of Tables

List of Figures

CHAPTER 1 Introduction

1.1 Observational History

The Crab Nebula supernova remnant is in the constellation of Taurus. It is one of the most studied astronomical objects and is widely accepted to be due to a supernova seen on July 4th 1054 A.D. by the Chinese astronomer Weide Yang and other Japanese, Korean and Arab astronomers. They reported sighting a new bright star in the sky. This "guest star", as the Chinese called it, was so brilliant that it was visible for almost three weeks during the daytime. The following review of the history draws heavily on Mitton (1980).

This supernova had not been remembered for six hundred years until the telescopes were invented. Many fainter objects can be detected with the help of the telescopes. In 1731 the English astronomer John Bevis, who had his own observatory at his house, discovered what we now call the Crab Nebula. Although Bevis did not publicize the event, he wrote to Charles Messier, a French astronomer, to draw his attention to this nebula in 1771. However, Messier probably had already observed this nebula by 1758.

Edmond Halley carefully studied and analyzed three bright comets observed in 1531, 1607 and 1582 and he demonstrated that all these three comets could be explained as the same moving object surrounding the Sun with a period of 76 years. Based on this he predicted that this object would return in 1758. Halley's work led comet hunting to be a very popular branch in observational astronomy.

Charles Messier was a famous comet discoverer in the 18th century and he discovered 16 comets. In 1758, in searching for Halley's predicted comet, he observed the Crab Nebula and considered it as comet predicted by Halley. After careful observations, he found that this object was not moving across the sky and concluded that it was not a comet. In the process of searching for true comets he

observed many nebulae. He decided to make a list of these objects of cloudy nature, but not moving in the sky, to avoid considering them incorrectly as comets. The Crab Nebula became the first object in Messier's catalogue, known as M1.

Although the publication of Messier's catalogue resulted in a great deal of further research on the Crab Nebula, few of them contributed significantly to an understanding of its nature. For example, the outstanding observer William Herschel tried to resolve the Crab Nebula into stars but he failed.

The third Earl of Rosse built a 36-inch telescope and used it to observe the Crab Nebula in 1844. This resulted in the current name of the Crab Nebula since his drawing of the nebula which was published in Philosophical Transactions of the Royal Society resembled a crab superficially.

From the early twentieth century, astronomers started connecting the Crab Nebula to the old historical records due to photographic and spectroscopic technologies. In 1921 Carl Lampland discovered changes in the structure of the Crab Nebula after he compared its photos taken over a period of 8. This was confirmed by John Duncan, working at Mount Wilson Observatory, several weeks later. Their research demonstrated that the nebula expanded from its center and the expansion began about 900 years ago. In 1928 Edwin Hubble was the first to suggest that the Crab Nebula is the remnant of a stellar explosion and noted that the only possible nova in its region was the one seen in 1054. Until 1942, it was Nicholas Mayall and Jan Oort that finally confirmed that the Crab Nebula is the remnant of the supernova explosion in 1054 recorded by the Chinese.

1.2 Introduction to Supernovae

1.2.1 Classification of Supernovae

In order to understand the supernovae, astronomers classified them according to their spectra as well as their light curves. Generally, there are two types of supernovae, Type I and Type II. Type I supernovae do not show any hydrogen lines in their spectra. The light curves of Type I supernovae exhibit sharp maxima and then fade away gradually. The peak could be ten billion solar luminosities. Conversely, the spectra of Type II supernovae contain strong hydrogen lines. The light curves of Type II supernovae have less sharp peaks at maxima and die away sharply. The maximum is about one billion solar luminosities. Type I supernovae can be subdivided into Type Ia, Type Ib (with He I λ5876) and Type Ic (without He I λ5876). Type II supernovae can be subdivided into Type II-P (with a "plateau" in light curves), Type II-L.

1.2.2 Spectra of Supernovae

Filippenko(1997) describes the spectra of different types of supernovae in both early-time and late-time. The early –time, around one week, spectra of supernovae are shown in Figure 1.1(Filippenko 1997). Spectra of Type Ia, Type II, Type Ic and Type Ib are shown as (a), (b), (c) and (d). SN 1987N(Ia) shows a deep Si II absorption line around 6150Å which is produced by blushifted Si II $\lambda\lambda$6347, 6371. SN 1984L(Ib) and SN 1987M(Ic) do not show this absorption feature.
Strong He I λ5876 lines exists in Type Ib and this distinguishes Type Ib from Type Ic. The late-time, longer than 4 months, spectra of supernovae illustrated in Figure 1.2. This gives more constraints on the classification scheme (Filippenko 1997). SN 1987N(Ia) shows blends of many Fe emission lines, mixed with some Co lines. For both Type Ib and Type Ic, strong emission lines of O, Ca and Mg are present. The spectra of Type II show similar features of Type Ib and Type Ic except the strong Hα line.

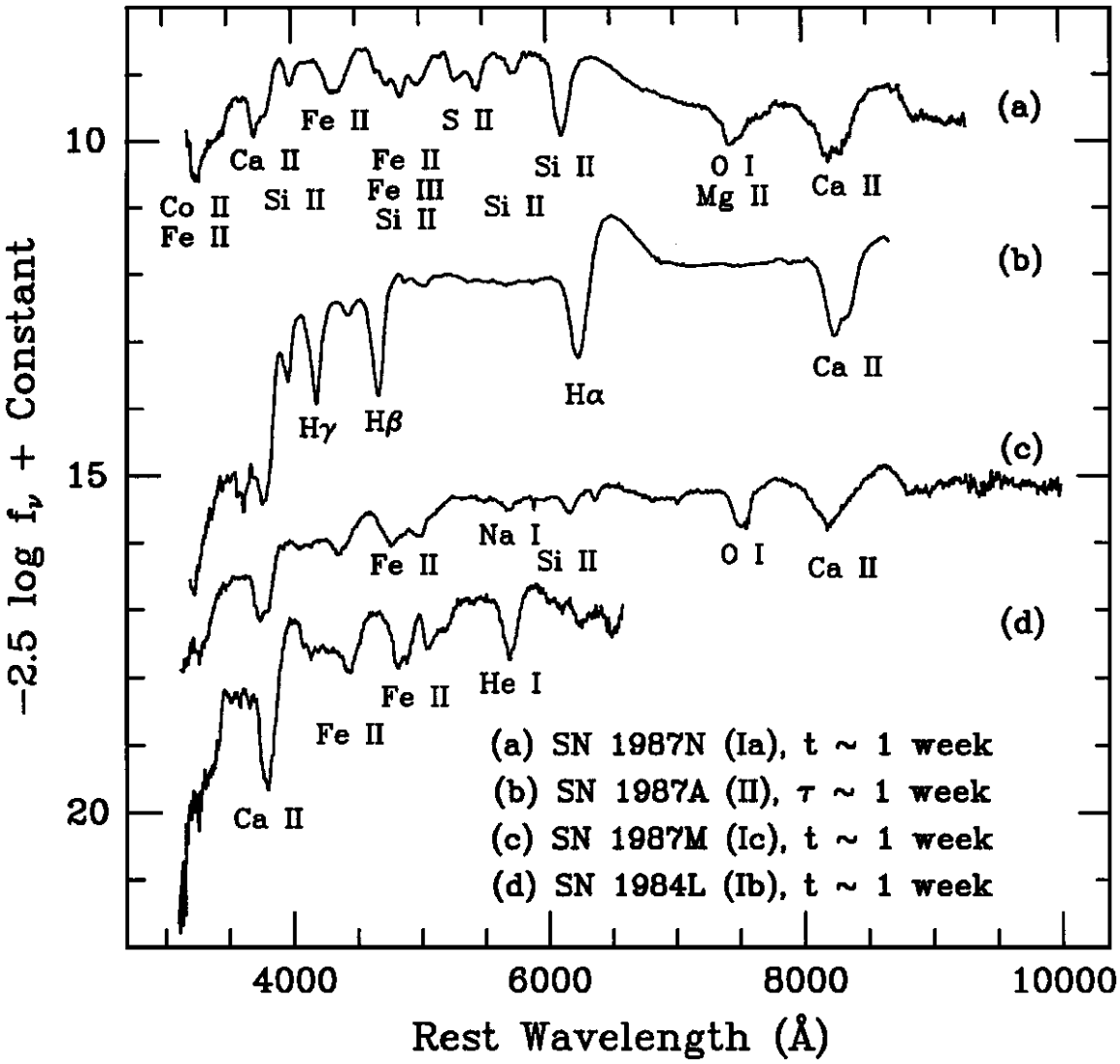

Figure 1.1 Spectra of four major types and subtypes of supernovae in their early times. (Taken from Filippenko 1997)

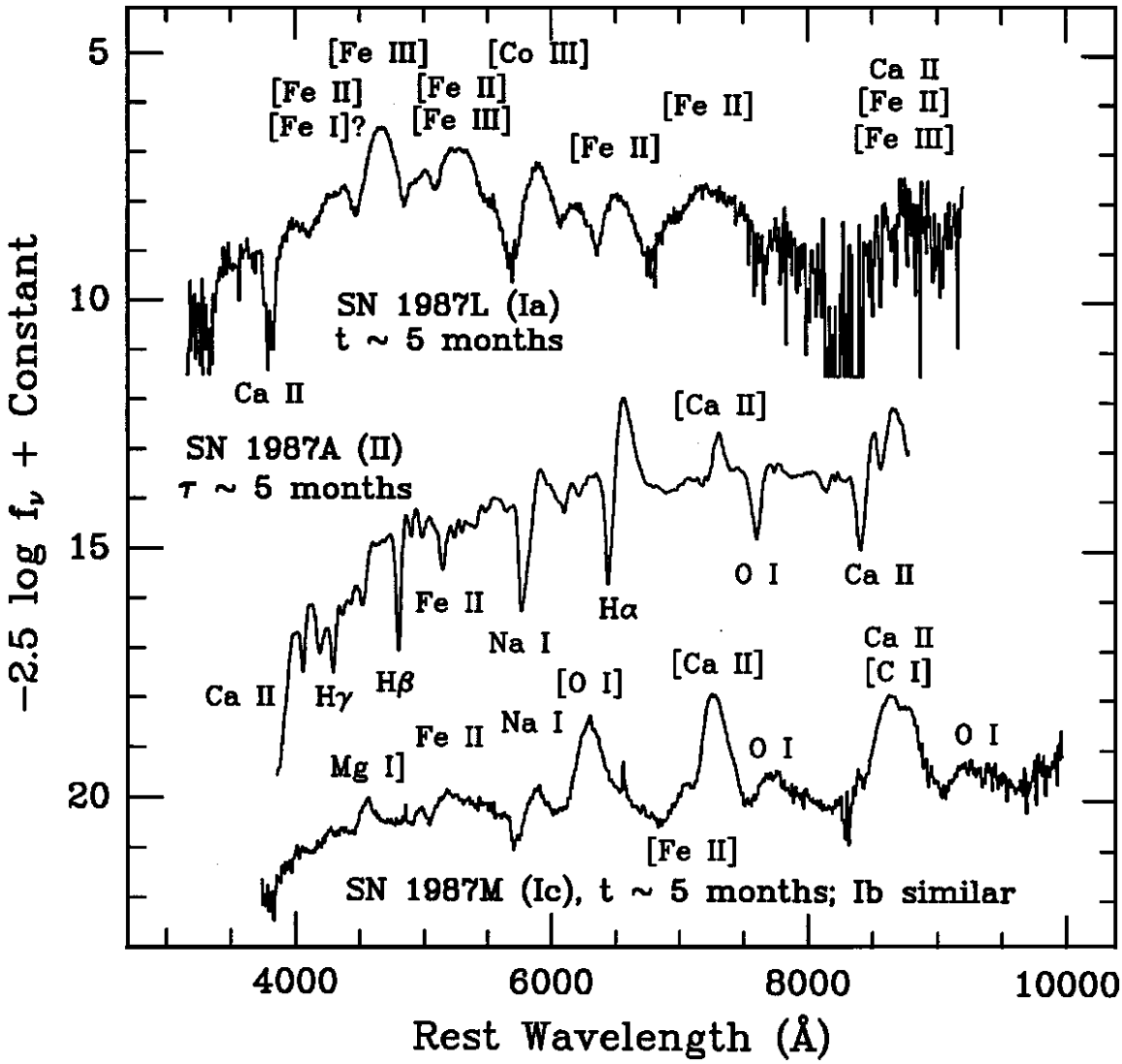

Figure 1.2 Spectra of four major types and subtypes of supernovae at late times. (Taken from Filippenko 1997)

1.2.3 Light Curves

Filippenko (1997) discusses the optical light curves at blue (B) wavelengths of different types of supernovae and they are shown in Figure 1.3. Generally, the light curves of Type I show many similarities whereas those of Type II exhibit much dispersion.

For Type Ia supernovae, The typical maximum brightness is M_B=-18.4. For Type Ib and Type Ic supernovae in blue light, the values are usually 1.5 to 2 smaller. (Carroll & Ostlie 2006). The brightness decline rates after peak for all Type I supernovae are similar, about 0.065 ($\pm$0.007) magnitude per day at 20 days (Carroll & Ostlie 2006). The decline rates slow down after about 50 days and become constant, with a rate of 50% faster for Type Ia than other subtypes.

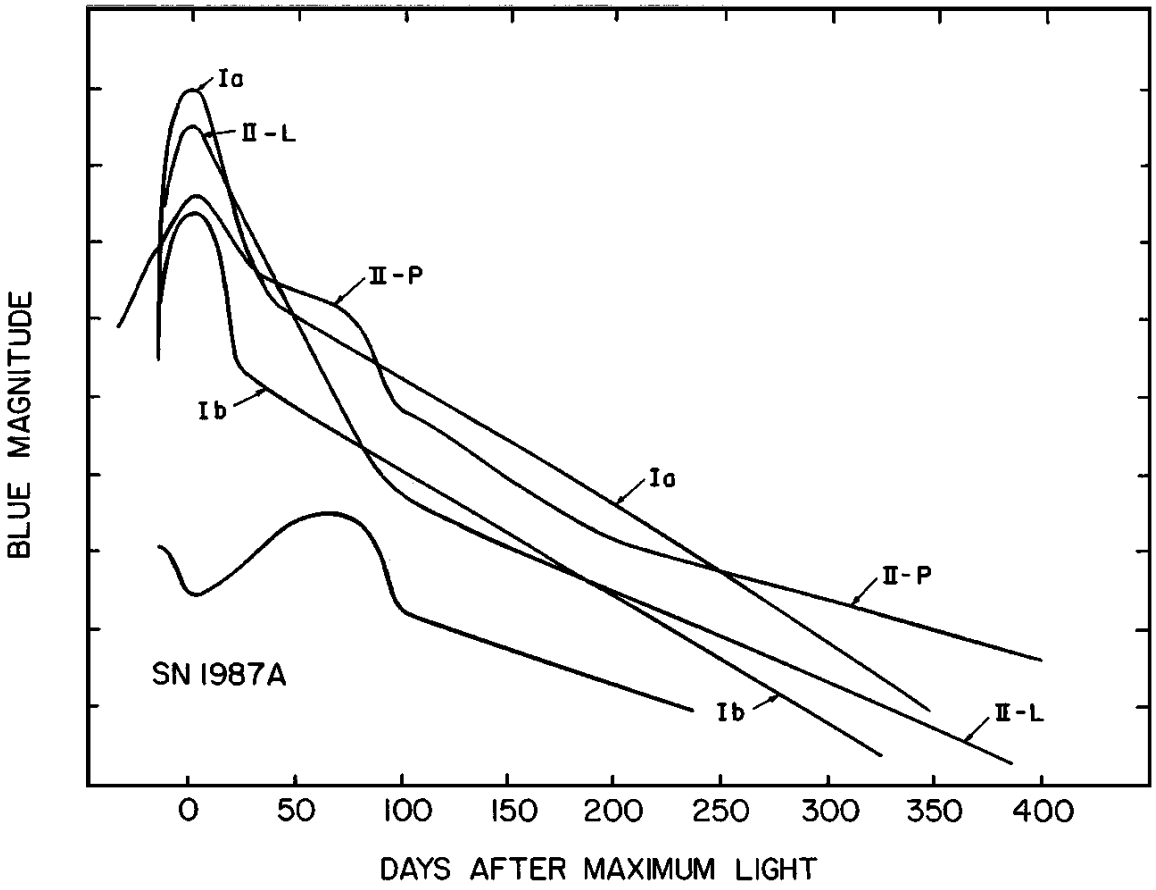

Figure 1.3 Light curves for different types of supernovae, including Type Ia, Type Ib, Type II-P and Type II-L. (Taken from Filippenko 1997)

For Type II supernovae, the peak brightness is typically 0.5 to 1.5 magnitudes fainter than that of Type Ia. After the peak the luminosity drops 6 to 8 magnitudes steadily in a year (Carroll & Ostlie 2006). The light curves of Type II supernovae show a variety of shapes and they can be subdivided into several subtypes. For Type

II-P's light curves, there is a plateau shown after the initial rise and decline in brightness, and this plateau phase could last up to three months before a slow decay. For Type II-L's light curves, no such plateau phase exists.

1.3 The Crab Nebula: physical conditions

1.3.1 Crab pulsar

The Crab pulsar, named PSR B0531 +21, is a very young neutron star, only 962 years old. It is first discovered by Comella et al. (1969) and Staelin & Reifensitein (1968) at radio wavelength in 1968, becoming the first identified pulsar that could be directly related to a supernova remnant. The Crab neutron star has a diameter of about 20 km, with a rotation period of 33 ms and a slowing down rate $\dot{P} = 4.21 \times 10^{-13}$(Hester 2008). Assuming the pulsar's mass M=1.4$M_{\rm sun}$, the spin-down luminosity of the Crab pulsar is $L_{spin} \cong 5 \times 10^{38}$ erg s^{-1}(Hester 2008). The spin-down luminosity is considered to be the energy source to power the whole Crab Nebula.

1.3.2 Synchrotron nebula

The synchrotron nebula is formed by protons and electrons and these particles are accelerated to relativistic speeds by the magnetic fields of the pulsar. It can be observed in many wavelength, from radio to X-ray. Figure 1.4 shows a composite image observed by different telescopes for the synchrotron nebula of the Crab Nebula (Hester 2008). The pulsar is shown as the blue point in the central of the image. The X-ray image in the inner regions shown in blue is taken by the Chandra X-ray Observatory (Hester et al. 2002). The optical image in the middle regions shown in green is obtained by the Hubble Space Telescope (Loll 2010). The radio image in the outer regions shown in red is observed by Very Large Arrays (Bietenholz & Kronberg 1990).

The structure of the synchrotron nebula can be explained by the term breaking frequency. The breaking frequency is defined as the frequency at the point where the synchrotron radiation losses exceeds the energy loss caused by the free-free radiation and adiabatic expansion (Loll 2010). It is defined by the following equation (Loll 2010):

$$v_{bf} = 10^{21} \left(\frac{B_{\mathrm{sn}}}{1\mu\mathrm{G}}\right)^{-3} \left(\frac{t}{10^3\mathrm{yr}}\right)^{-2} \mathrm{Hz} \qquad (1.1)$$

where B_{sn} is the magnetic field of the synchrotron nebula.

Figure 1.4 A composite image of the synchrotron nebula of the Crab nebula taken by Chandra, HST and VLA. (taken from Hester 2008)

Particles with frequencies larger than the breaking frequency can only travel a short distance from the central of the nebula by radiating their energy very rapidly and never arrive to the edge of the Crab (Gaensler & Slane 2006). But particles with smaller frequencies than the breaking frequency can travel farther. This is the reason that the X-ray image is only seen in the inner regions of the synchrotron

nebula while the radio image extends to the much farther outer regions of the synchrotron nebula.

1.3.3 Thermal filaments

The thermal filaments are the structures which produce the emission lines. The filaments are formed by the ejecta of the supernova and contain most of the observable mass of the Crab Nebula. The thickness of the thermal filaments is about 0.01 pc and the distances between the Crab pulsar and almost all the filaments are longer than 0.5 pc (Davidson & Fesen 1985). The thermal filaments, in three dimensions, are confining the synchrotron nebula in a 2.1×1.4 pc diameter ellipsoid (Davidson & Fesen 1985). The outer boundary of the ellipsoid defined by the fainter extended filaments is in the dimension of 3.8×2.9 pc (Davidson & Fesen 1985). Clark et al. (1983) obtains the expansion velocities of the thermal filaments vary from 700∼1800 km s^{-1}, with a characteristic value of 1500 km s^{-1} at the edge of the observable nebula.

Figure 1.5 shows the composite image of the Crab Nebula obtained the by Hubble Space Telescope (Hester 2008). It shows that the filaments formed by the supernova ejecta surround the visible synchrotron nebula shown in blue color. The Crab Nebula does not only include emission lines which are seen in typical nebulae, such as forbidden lines [N II], [O III], [O II], and recombination lines He I, He II and H I, but also contains strong [Ne V], [S II] and [O I] (Osterbrock & Ferland 2006). In Figure 1.5, the filaments shown in blue in the inner regions of the filaments indicate the emission line of [O I] λ6300 (Hester 2008). [S II] $\lambda\lambda$6717, 6731 is shown in green in the middle regions while [O III] λ5007 shown in red is observed in the outer regions of the filaments (Hester 2008). The line ratios between the above forbidden lines are good indicators of the density and temperature. For example, the line ratios of [O II] $\lambda\lambda$3726, 3729 and [S II] $\lambda\lambda$6716, 6731 indicate that the measured filaments have electron densities around 10^3 cm^{-3} (Osterbrock & Ferland 2006). The line ratio [O III] (λ4959+λ5007)/λ4363 indicates a temperature about 15000 K

(Osterbrock & Ferland 2006). The line ratio [N II] (λ6548+λ6583)/λ5755 gives a mean temperature around 7400 K (Osterbrock & Ferland 2006).

1.3.4 H_2 emission in the Crab Nebula

Observations show that strong H_2 lines are emitted from the Crab Nebula (Graham et al. 1990; Loh et al. 2010; Loh et al. 2011; Loh et al. 2012). To understand this, we need to focus on the ratio of H_2 2.121 μm line to the nearby H I lines.

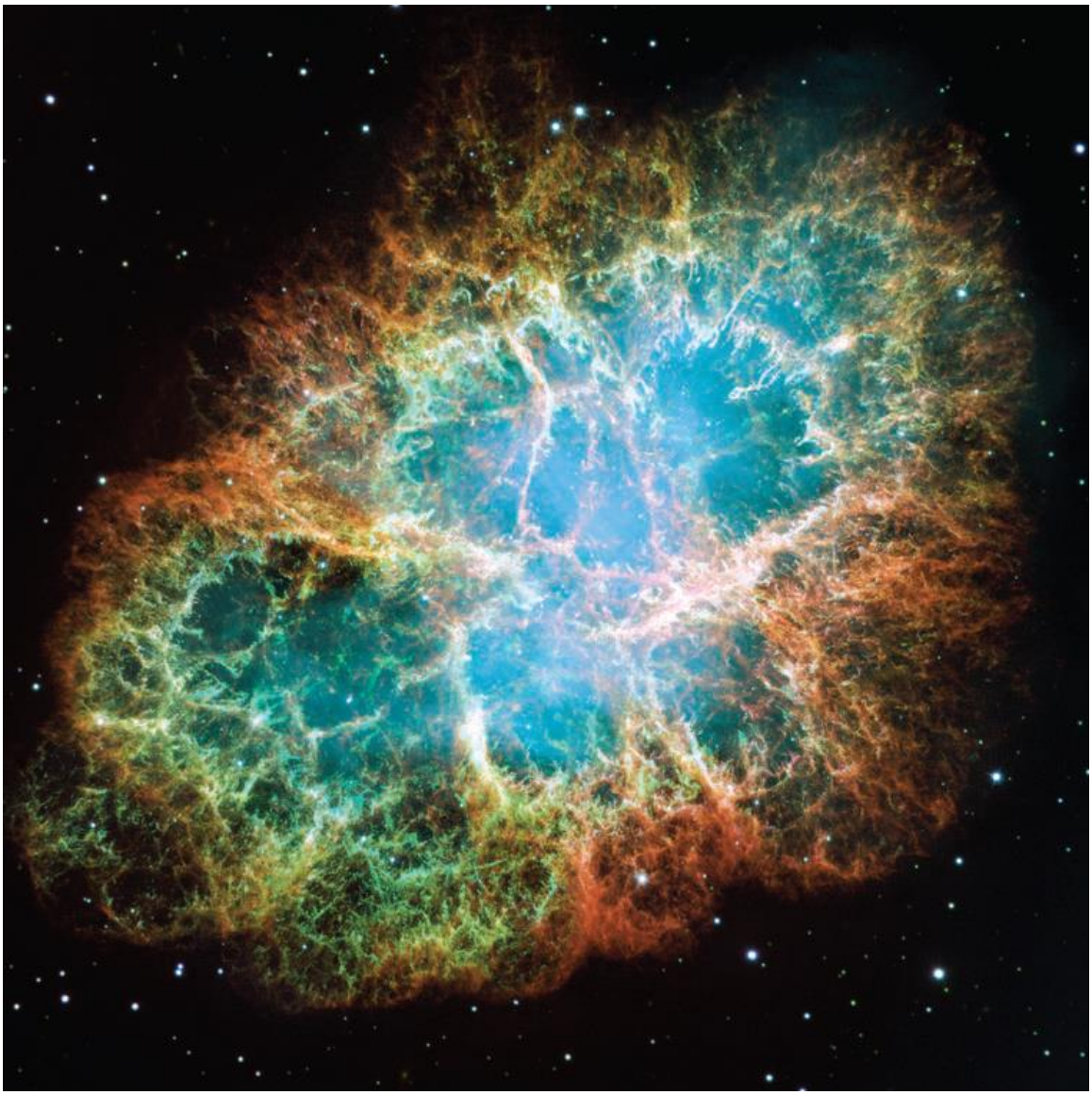

Figure 1.5 A composite image of the Crab Nebula obtained from Hubble Space Telescope. (taken from Hester 2008)

The H I line comes from the recombination from the ionized gas regions which are usually ionized by nearby stars or AGNs. The H I line intensities are proportional to the numbers of photons which are able to ionize hydrogen emitted from the nearby stars or AGNs (Osterbrock & Ferland 2006). Because the SED of these stars and AGNs has a maximum value at the energies which can ionize hydrogen, H I recombination lines in such environments are very strong (Ferland 2011).

For H_2, since the energy separations of the energy level, vibrational levels and rotational levels, are wide, the emission lines are very difficult to form and are faint (Ferland 2011). In a typical PDR or H II region, H_2 only exists in relatively cold regions where self-shielding could prevent photo-dissociations. Thus strong H_2 emission is produced by fluorescence excitation while collisional excitation is very weak (Osterbrock & Ferland 2006). As a result, H_2 emission is much fainter than the H I emission and the line ratio of H_2/H I is very small. Figure 1.6 shows the ratios of H_2/H I in different objects, as well as the ratio of [Fe II]/H I (Riffel et al. 2010). The ratio of H_2/H I is small in Orion (H II region) due to the reason discussed above.

Figure 1.6 also shows that the line ratio of H_2/H I is high in the Crab Nebula. Graham et al. (1990) detected the H_2 1-0 S(1) line at two of three observed locations in the Crab Nebula. Loh et al. (2010) detected strong H_2 emission in seven knots within the Crab Nebula by using the Spartan Infrared camera on the SOAR Telescope and found ratio of the H_2/H I is very high. Loh et al. (2011) discovered that 55 knots in the Crab filaments emit strong H_2 1-0 S(1) line. Loh et al. (2012) obtained that the H_2 excitation temperature to be very high, around 2000 K to 3000 K, in six knots in the Crab.

The H_2 in the Crab Nebula appears to be very warm, indicating a high gas kinetic temperature. However, the mechanism producing these strong H_2 emission is unlikely to be fluorescent processes or grain formation pumping mentioned before. The easiest way to produce such strong H_2 emissions in such warm environment is collisional excitation, which could make very strong emissions if the temperature is high enough (Ferland 2011; Richardson et al. 2013). If the gas density is high enough for the gas to be in LTE then the level excitation temperature would equal to the gas temperature and the H_2 emission could be used to measure the mass of the gas. However, there is no way to measure the density directly and only the level population diagram is the tool to use. Chapter 3 of this dissertation gives a detailed study on the level population diagram and its indications.

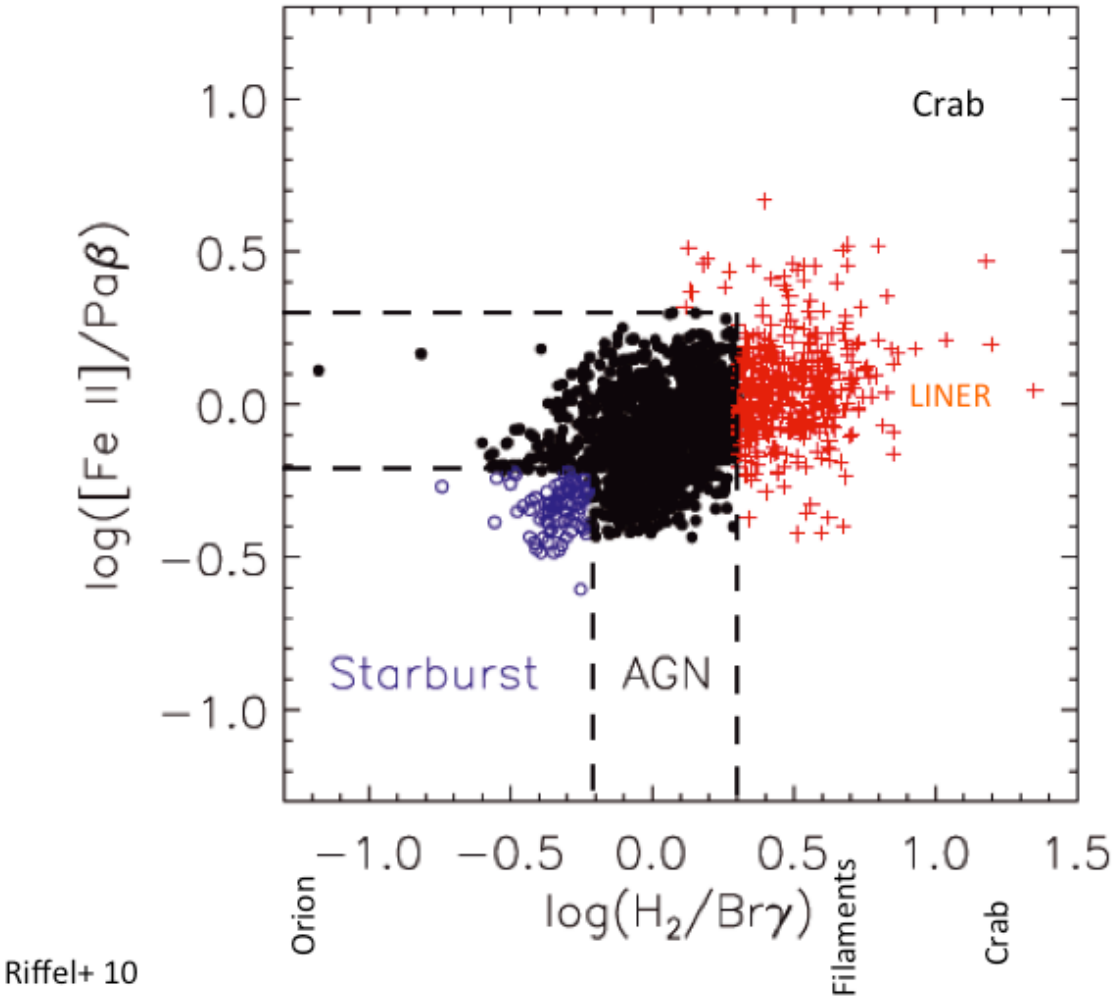

Figure 1.6 Line ratios of H_2 to H I in different astronomical objects. (taken from Riffel et al. 2010)

1.4 Unseen outer shell of the Crab Nebula

The Crab Nebula is generally considered to be a core-collapse supernova remnant for two reasons: hydrogen lines are shown in its spectrum and it has a central neutron star (pulsar). However, several facts, mainly its total mass and kinetic energy, are not compatible with a normal core-collapse supernova. The mass of the Crab pulsar is around 1.4 $M_{\rm sun}$ and the total mass of the ejecta of Crab Nebula is between 2-5 $M_{\rm sun}$ (Fesen et al. 1997; Davidson & Fesen 1985). The total mass is much less than the mass of the progenitor of the Crab Nebula, 8-13 $M_{\rm sun}$, suggested

by Nomoto (1985, 1987) and the more recent model by Kitaura et al. (2006). Also, the kinetic energy of the Crab Nebula is of the order of 10^{49} erg, which is significantly smaller than 10^{51} erg, the value of a typical core-collapse supernova.

1.4.1 Predictions of the unseen outer shell

It was suggested that something had not been observed for the Crab Nebula since both the observed mass and the kinetic energy are less that what they should be. It was first suggested by Chevalier (1977) that an outer unseen shell, containing the missing mass and kinetic energy, is surrounding the visible Crab Nebula. Lundqvist et al. (1986) uses time-dependent photoionization models to calculate such a rapidly expanding outer shell. Their models predicted that the outer shell could be detected in several UV absorption lines, including the C IV $\lambda 1550$. Sankrit & Hester (1997)'s models include both photoionization and a shock-heated outer shell. In contrast, Smith (2013) explains the Crab as a type of under-luminous supernova, without including an unseen outer shell. Wang et al. (2013) uses CLOUDY (Ferland et al. 2013) to present several time independent photoionization models for the unseen outer shell and this work is part of this dissertation (Chapter 2). Wang et al. (2013) found that very strong infrared coronal lines are the best hope to detect the unseen outer shell, especially the [Ne VI] $\lambda 7.652$ μm.

1.4.2 Observational detections of the unseen outer shell

Observers have been searching the unseen outer shell for over thirty years. Lundqvist & Tziamtzis (2012) summarizes these searches by wavelengths. The searches in radio wavelengths include Wilson & Weiler (1982), Velusamy (1984, 1985), Trushkin (1986), Velusamy et al. (1992) and Frail et al. (1995). The searches in optical wavelengths have been done by Fesen & Ketelsen (1985) and Fesen et al. (1997). The searches have also been performed in X-rays, such as Mauche & Gorenstein (1985), Predehl & Schmitt (1995) and Seward et al. (2006). However, none of the searches above obtained positive results. Murdin & Clark (1981) and

Murdin (1995) report that a shell outside the visible Crab Nebula is detected directly but this result could not be confirmed by searches with better observational limits (Fesen et al. 1997; Fesen 1997).

The only direct evidence of the unseen outer shell was from Sollerman et al. (2000). They observed the Crab Nebula in far-UV with the Hubble Space Telescope. They observed weak blueshifted absorption feature from the C IV λ1550, with the maximum blueward velocity around 2500 km s^{-1}. They explained this as a direct evidence of an outer shell surrounding the visible Crab predicted by Chevalier (1977). However, Sollerman et al. (2000) fails to detect any materials with velocities higher than 2500 km s^{-1}. Also, the missing mass detected by Sollerman et al. (2000) is only about 0.3 M_{sun} and the kinetic energy is only about 1.5×10^{49} ergs. These values are much less than what they are expected to be for a reasonable outer shell.

CHAPTER 2 Detecting the rapidly expanding outer shell of the Crab Nebula: where to look

2.1 Introduction

The Crab Nebula is generally thought to have been produced by a core collapse supernova. The total mass in the observed ejecta is 2-5 M_{sun} (Davidson & Fesen 1985; Fesen, Shull & Hurford 1997) and the pulsar should have a mass of about 1.4M_{sun} (Davidson & Fesen 1985). This is much less than the total mass of 8-13 M_{sun} (Nomoto 1985, 1987; Kitaura, Janka & Hillebrandt 2006) thought to be in the star before the explosion. Thus the long-standing problem, where is the missing mass? The possibility most often discussed is that it lies within an unseen outer shell, sometimes referred to as the Crab's halo. The literature on this is comprehensive, with Lunqdvist & Tziamtzis (2012) and Smith (2013) giving good summaries of the current situation. Smith (2013) discusses an alternative explanation, that the Crab was a type of under-luminous supernova.

There have been only a few predictions of the detailed spectrum of the outer shell. Lundqvist, Fransson & Chevalier (1986) did time-dependent numerical simulations of the spectrum with a constant density structure and Sankrit & Hester (1997) predict some properties of a photoionized and shock heated shell. Here we use an up-to-date atomic database in the spectral synthesis code Cloudy (Ferland et al. 2013) to compute emission and absorption spectra. We largely confirm previous estimates of the hydrogen emission but find that strong optical and infrared coronal lines should also be present. We identify promising lines in the IR that would be a robust indicator of the presence of this outer shell.

2.2 Parameters of the outer shell

The total luminosity of the Crab Nebula, and its spectral energy distribution (SED), are well known (Davidson & Fesen 1985). Although other energy sources such as shocks may be present (Sankrit & Hester 1997), photoionization by this continuum

must occur (the SED is observed) and by itself can power the outer shell. Shock heating would only add to this. To compute a photoionization model of the outer shell and its spectrum we must specify the gas composition, its density, and how the density varies with radius.

We assume that the outer shell is an inhomogeneous shell with an uncertain outer radius, but with an inner radius equal to the outer radius of the familiar Crab, R_{in}= 5.0×10^{18} cm (Sankrit & Hester 1997). The expansion velocity at the inner radius v_{in} is roughly 1680 km s^{-1} at this radius (the Crab is, of course, not a sphere, so this is a simplification).

A velocity gradient must be present, since the outer shell lies outside the familiar Crab. We consider both a Hubble flow, with $v(r) \propto r$, and an arbitrary velocity law as a sensitivity test, with $v(r) \propto r^2$. We obtain two different density laws from these two velocity distributions and apply them in this paper to check how predictions depend on this assumption.

The total mass in the outer shell may be of order 4 to 8 M_{sun} (Sollerman et al. 2000). We assume $4M_{sun}$ recommended by Sollerman et al. (2000), which we show below is consistent with limits to the line surface brightness (Fesen, Shull & Hurford 1997; Tziamtzis et al. 2009). We combine this with the three power laws given above to find the gas density as a function of radius.

2.2.1 The outer radius

We will determine the gas density by combining the total mass with the density law and the inner and outer radii. The outer radius is unknown but must be specified to determine the gas density. Given our assumptions about the radius – velocity law, the outer radius corresponds to a particular highest expansion velocity. Chevalier (1977) gives a range of expansion velocities between 5,000 km s^{-1} and 10,000 km s^{-1}, Lundqvist, Fransson & Chevalier (1986) give a maximum expansion velocity of

5,000 km s^{-1}, Sankrit & Hester (1997) assume a maximum velocity of 10,000 km s^{-1}, and Sollerman et al. (2000) quote 6370 km s^{-1}. We assume the velocity at the outer radius v_{out} = 6370 km s^{-1}, a velocity ~3.8 times larger than the expansion of the observed nebula, and give results relative to this velocity. The $v(r) \propto r$ Hubble flow results in

$$R_{out} \approx 3.8 R_{in} = 1.9 \times 10^{19} [\text{cm}]. \quad (2.1)$$

while for the $v(r) \propto r^2$ expansion law the outer radius is

$$R_{out} \approx 1.9 R_{in} = 9.5 \times 10^{18} [\text{cm}]. \quad (2.2)$$

2.2.2 The density law

For the spectroscopic simulations we need to set the outer shell density n_0 at its inner edge R_{in}, the density law $n(r) \propto r^{\alpha}$, and the outer radius R_{out}. We investigate two density laws here, $\alpha = -3$ and $\alpha = -4$. The density law is determined by two quantities, how the expansion velocity varies with radius, $v(r) \propto r^{\gamma}$, and how the mass flux varies with radius, $MF \propto r^{\beta}$. We consider three cases, summarized in Table 1, as follows:

(I) The simplest case is a Hubble-law expansion, the sudden release of mass with a range of velocities so that $\gamma = 1$ and $v \propto r$. For the mass flux, the simplest assumption is that the initial density distribution is constant, so that

$$MF = 4\pi r^2 n(r) v(r) \propto 4\pi r^{2+\alpha+\gamma} = 4\pi r^{\beta} \quad (2.3)$$

is constant. Since $\gamma = 1$, if $\alpha = -3$, then $\beta = 0$, indicating mass flux conservation.

(II) As the second case we still assume that the Hubble velocity law is maintained so that $\gamma = 1$ and $v \propto r$. If $\alpha = -4$, then $\beta = -1$, meaning that the mass flux decreases with increasing radius. This may happen if the outer layer of the star had a lower density.

(III) As a third case we also consider $\alpha = -4$. As a sensitivity test, we will also test

an arbitrarily different velocity law expansion with $\gamma = 2$ and $v(r) \propto r^2$. In this case we also obtain $\beta = 0$, that is, the mass flux is conserved.

The density law for case I is

$$n(r) = n_0(\frac{r}{R_{in}})^{\alpha} = n_0 \left(\frac{r}{R_{in}}\right)^{-3} [\mathrm{cm}^{-3}] \tag{2.4}$$

and for case II and case III is

$$n(r) = n_0 \left(\frac{r}{R_{in}}\right)^{-4} [\mathrm{cm}^{-3}]. \tag{2.5}$$

2.2.3 The shell mass and inner density

We can calculate n_0 by mass conservation,

$$M_{halo} = 4\pi \int_{R_{in}}^{R_{out}} m\, n_0 \left(\frac{r}{R_{in}}\right)^{\alpha} r^2 dr \ [\mathrm{gm}]. \tag{2.6}$$

Here M_{halo} is the total mass of the outer shell and m is the mass per hydrogen for the assumed composition. Note that the composition of a supernova remnant is usually different in different parts, therefore we assume three different compositions for the outer shell: the abundances of some of the Crab filaments (Pequignot & Dennefield 1983), solar abundances (recommended by Sollerman et al. 2000), and ISM abundances (which are basically solar with grains). If μ is the mass of the proton then $m = 3.8\mu$ for the enhanced Crab abundances derived by Pequignot & Dennefield (1983) and $m = 1.4\mu$ for solar and ISM abundances. A list of assumed abundances is given in table 3a in Pequignot & Dennefield (1983). We obtain the following expression for n_0 with the middle value $m = 2.6\mu$ and $M_{halo} = 4\ M_{sun}$

$$n_0 = \frac{M_{halo}}{4\pi m R_{in}^3 \ln \frac{R_{out}}{R_{in}}}$$

$$= 0.87 \frac{2.6\mu}{m} \frac{M_{halo}}{4M_{sun}} \frac{\ln 3.8}{\ln \frac{R_{out}}{R_{in}}} [\mathrm{cm}^{-3}][\mathrm{erg}], \quad \text{case I;} \tag{2.7}$$

$$n_0 = \frac{M_{halo}}{4\pi m R_{in}^3 \left(1 - \frac{R_{in}}{R_{out}}\right)}$$

$$= 1.58 \frac{2.6\mu}{m} \frac{M_{halo}}{4M_{sun}} \frac{0.74}{1-\frac{R_{in}}{R_{out}}} [\mathrm{cm}^{-3}][\mathrm{erg}], \quad \text{case II;} \tag{2.8}$$

$$n_0 = \frac{M_{halo}}{4\pi m R_{in}^3 \left(1 - \frac{R_{in}}{R_{out}}\right)}$$

$$= 2.46 \frac{2.6\mu}{m} \frac{M_{halo}}{4M_{sun}} \frac{0.47}{1-\frac{R_{in}}{R_{out}}} [\mathrm{cm}^{-3}][\mathrm{erg}], \quad \text{case III;} \tag{2.9}$$

We see that the density depends on both the inner radius and the outer radius for the $\alpha = -3$ law. This is important because the density determines the emission measure of the lines, and this depends on the uncertain outer radius. For the case of $\alpha = -4$, the density depends only on the inner radius if the outer radius is much larger than the inner radius. Table 5 in Sollerman et al. (2000) also gave the densities in the inner edge for different density laws.

2.2.4 Kinetic energy

Before proceeding with the model we derive the kinetic energy for each of these hypotheses. The kinetic energy of the filaments is about 3×10^{49} ergs (Hester 2008), which is far less than the canonical 10^{51} ergs seen in the ejecta of core collapse supernovae (Davidson & Fesen 1985). We calculate the kinetic energy in the outer shell to check if this makes up the missing energy. We obtain the kinetic energy of the outer shell

$$E_k = 6.86 \times 10^{50} \frac{M_{halo}}{4M_{sun}} \frac{\ln 3.8}{\ln \frac{R_{out}}{R_{in}}} \frac{\left(\frac{R_{out}}{R_{in}}\right)^2 - 1}{13.44} [\mathrm{erg}], \quad \text{case I;} \tag{2.10}$$

$$E_k = 4.26 \times 10^{50} \frac{M_{halo}}{4M_{sun}} \frac{0.74}{1-\frac{R_{in}}{R_{out}}} \frac{\frac{R_{out}}{R_{in}}-1}{2.8} [\text{erg}], \quad \text{case II;} \tag{2.11}$$

$$E_k = 6.70 \times 10^{50} \frac{M_{halo}}{4M_{sun}} \frac{0.47}{1-\frac{R_{in}}{R_{out}}} \frac{\left(\frac{R_{out}}{R_{in}}\right)^3-1}{6.38} [\text{erg}], \quad \text{case III.} \tag{2.12}$$

These provide about half of the missing energy, which is within the uncertainty in our assumed shell parameters. Table 5 in Sollerman et al. (2000) also gave the kinetic energies of the outer shell for different density laws.

The next step is to predict the full emission and absorption line spectra of the outer shell using photoionization models.

2.2.5 Emission measure and line luminosity

We obtain the luminosities of emission lines from the numerical calculations presented below. We use H I line emissivities given by Osterbrock & Ferland (2006) and Ferland (1980). The luminosity of Hβ is

$$L(\text{H}\beta) = \int \frac{4\pi j_{\text{H}\beta}}{n_e n_p} n(r)^2 dV \tag{2.13}$$

$$\approx \frac{4\pi j_{\text{H}\beta}}{n_e n_p} \times \ EM \ [\text{erg s}^{-1}] \tag{2.14}$$

where $\frac{4\pi j_{\text{H}\beta}}{n_e n_p}$ is the H I Case B recombination coefficient (Osterbrock & Ferland 2006). EM is the volume emission measure, defined as

$$EM = \int n(r)^2 dV \tag{2.15}$$

$$\approx \int \left[n_0 \left(\frac{r}{R_{in}}\right)^{\alpha} \right]^2 dV \ [\text{cm}^{-3}] \tag{2.16}$$

corresponding to

$$EM = \frac{4}{3}\pi n_0^2 R_{in}^3 \left[1 - \left(\frac{R_{in}}{R_{out}}\right)^3\right]$$

$$= 3.89 \times 10^{56} \left(\frac{2.6\mu}{m}\right)^2 \left(\frac{M_{halo}}{4M_{sun}}\right)^2 \left(\frac{ln3.8}{ln\frac{R_{out}}{R_{in}}}\right)^2 \frac{\left[1-\left(\frac{R_{in}}{R_{out}}\right)^3\right]}{0.98} [\text{cm}^{-3}] \text{ case I;} \tag{2.17}$$

$$EM = \frac{4}{5}\pi n_0^2 R_{in}^3 \left[1 - \left(\frac{R_{in}}{R_{out}}\right)^5\right]$$

$$= 7.86 \times 10^{56} \left(\frac{2.6\mu}{m}\right)^2 \left(\frac{M_{halo}}{4M_{sun}}\right)^2 \left(\frac{0.74}{1-\frac{R_{in}}{R_{out}}}\right)^2 \frac{\left[1-\left(\frac{R_{in}}{R_{out}}\right)^5\right]}{0.99} [\mathrm{cm}^{-3}] \text{ case II;} \quad (2.18)$$

$$M = \frac{4}{5}\pi n_0^2 R_{in}^3 \left[1 - \left(\frac{R_{in}}{R_{out}}\right)^5\right]$$

$$= 1.82 \times 10^{57} \left(\frac{2.6\mu}{m}\right)^2 \left(\frac{M_{halo}}{4M_{sun}}\right)^2 \left(\frac{0.47}{1-\frac{R_{in}}{R_{out}}}\right)^2 \frac{\left[1-\left(\frac{R_{in}}{R_{out}}\right)^5\right]}{0.96} [\mathrm{cm}^{-3}] \text{ case III.} \quad (2.19)$$

Therefore we find the final expressions of the luminosity for Hβ

$$L(\mathrm{H}\beta) = 1.43 \times 10^{31} \left(\frac{T}{2.9 \times 10^4}\right)^{-1.20} \left(\frac{2.6\mu}{m}\right)^2 \left(\frac{M_{halo}}{4M_{sun}}\right)^2 \times$$

$$\left(\frac{ln3.8}{ln\frac{R_{out}}{R_{in}}}\right)^2 \frac{\left[1-\left(\frac{R_{in}}{R_{out}}\right)^3\right]}{0.98} [\mathrm{erg\ s}^{-1}], \quad \text{case I;} \quad (2.20)$$

$$L(\mathrm{H}\beta) = 4.55 \times 10^{31} \left(\frac{T}{2.3 \times 10^4}\right)^{-0.833} \left(\frac{2.6\mu}{m}\right)^2 \left(\frac{M_{halo}}{4M_{sun}}\right)^2 \times$$

$$\left(\frac{0.74}{1-\frac{R_{in}}{R_{out}}}\right)^2 \frac{\left[1-\left(\frac{R_{in}}{R_{out}}\right)^5\right]}{0.99} [\mathrm{erg\ s}^{-1}], \quad \text{case II;} \quad (2.21)$$

$$L(\mathrm{H}\beta) = 1.20 \times 10^{32} \left(\frac{T}{2 \times 10^4}\right)^{-0.833} \left(\frac{2.6\mu}{m}\right)^2 \left(\frac{M_{halo}}{4M_{sun}}\right)^2 \times$$

$$\left(\frac{0.47}{1-\frac{R_{in}}{R_{out}}}\right)^2 \frac{\left[1-\left(\frac{R_{in}}{R_{out}}\right)^5\right]}{0.96} [\mathrm{erg\ s}^{-1}], \quad \text{case III;} \quad (2.22)$$

where we suppose the temperature to be in the neighborhood of 2.9×10^4K for case I, 2.3×10^4K for case II, and 2×10^4K for case III as computed below, and use the temperature power-law fit to $\frac{4\pi j_{\mathrm{H}\beta}}{n_e n_p}$ given by Ferland (1980). This is approximate due to the assumption of Case B H I emission. We show below that the Lyman lines

are not optically thick, and that continuum fluorescent excitation is important.

2.2.6 Scale radius

We can convert emission-line luminosities into surface brightness by dividing the luminosity by the area of emission on the sky. We assume that the lines form over a scale height determined by an effective radius, R_{eff}. The effective radius is defined as the position where half of the total line luminosity is formed. Emission line luminosities are determined by the emission measure, n^2V (Osterbrock & Ferland 2006), so the inner highest-density regions are most important. We obtain the effective or "half luminosity" radius from

$$\int_{R_{in}}^{R_{eff}} \frac{4\pi j_{\mathrm{H}\beta}}{n_e n_p} n(r)^2 \, dV = L/2[\mathrm{erg\ s^{-1}}]. \tag{2.23}$$

If we move $\frac{4\pi j_{\mathrm{H}\beta}}{n_e n_p}$ out of the integral, equivalent to assuming that the temperature is constant, we find

$$\left.\begin{aligned} R_{eff} &= R_{in}\left(\frac{2}{1+\left(\frac{R_{in}}{R_{out}}\right)^3}\right)^{\frac{1}{3}} \\ &= 6.26\times10^{18}\frac{\left(\frac{2}{1+\left(\frac{R_{in}}{R_{out}}\right)^3}\right)^{\frac{1}{3}}}{1.25}[\mathrm{cm}] \\ &= 1.25\,R_{in} \end{aligned}\right\} \text{ case I and case II;} \tag{2.24}$$

$$\left.\begin{aligned} R_{eff} &= R_{in}\left(\frac{2}{1+\left(\frac{R_{in}}{R_{out}}\right)^5}\right)^{\frac{1}{5}} \\ &= 5.67\times10^{18}\frac{\left(\frac{2}{1+\left(\frac{R_{in}}{R_{out}}\right)^5}\right)^{\frac{1}{5}}}{1.13}[\mathrm{cm}] \\ &= 1.15R_{in} \end{aligned}\right\} \text{case III.} \qquad (2.25)$$

2.2.7 Average surface brightness in H I recombination lines

We convert the luminosities given above into surface brightness averaged over the full outer shell as it would be seen projected on the sky, in order to compare the results with observations. We obtain the surface brightness

$$S(\mathrm{H}\beta) = \frac{1}{k^2}\frac{L}{4\pi^2 R_{eff}^2}\ [\mathrm{erg\ s^{-1}\ cm^{-2}\ arcsec^{-2}}] \qquad (2.26)$$

corresponding to

$$S(\mathrm{H}\beta) = 2.76\times10^{-19}\left(\frac{T}{2.9\times10^4}\right)^{-1.20}\left(\frac{2.6\mu}{m}\right)^2\left(\frac{M_{halo}}{4M_{sun}}\right)^2\left(\frac{ln3.8}{ln\frac{R_{out}}{R_{in}}}\right)^2\times$$

$$\frac{\left[1-\left(\frac{R_{in}}{R_{out}}\right)^3\right]}{0.98}\frac{1.25}{\left[\frac{2}{1+\left(\frac{R_{in}}{R_{out}}\right)^3}\right]^{\frac{1}{3}}}[\mathrm{erg\ s^{-1}\ cm^{-2}\ arcsec^{-2}}],\quad \text{case I;} \qquad (2.27)$$

$$S(\mathrm{H}\beta) = 9.42\times10^{-19}\left(\frac{T}{2.3\times10^4}\right)^{-0.833}\left(\frac{2.6\mu}{m}\right)^2\left(\frac{M_{halo}}{4M_{sun}}\right)^2\left(\frac{0.74}{1-\frac{R_{in}}{R_{out}}}\right)^2\times$$

$$\frac{\left[1-\left(\frac{R_{in}}{R_{out}}\right)^5\right]}{0.99}\frac{1.15}{\left[\frac{2}{1+\left(\frac{R_{in}}{R_{out}}\right)^5}\right]^{\frac{1}{5}}}[\text{erg s}^{-1}\text{ cm}^{-2}\text{ arcsec}^{-2}],\quad \text{case II;} \tag{2.28}$$

and

$$S(\text{H}\beta) = 2.17\times10^{-18}\left(\frac{T}{2\times10^4}\right)^{-0.833}\left(\frac{2.6\mu}{m}\right)^2\left(\frac{M_{halo}}{4M_{sun}}\right)^2\left(\frac{0.47}{1-\frac{R_{in}}{R_{out}}}\right)^2\times$$

$$\frac{\left[1-\left(\frac{R_{in}}{R_{out}}\right)^5\right]}{0.96}\frac{1.15}{\left[\frac{2}{1+\left(\frac{R_{in}}{R_{out}}\right)^5}\right]^{\frac{1}{5}}}[\text{erg s}^{-1}\text{ cm}^{-2}\text{ arcsec}^{-2}],\quad \text{case III;} \tag{2.29}$$

where k = 206265 converts luminosity into surface brightness. Table 5 in Sollerman et al. (2000) and Tziamtzis et al. (2009) also gave the surface brightness of the outer shell for different density laws.

The upper limit to the Hβ surface brightness corresponds to an upper limit to the mass in the shell, for a given power-law index. The composition also affects $S(\text{H}\beta)$ because, for Crab abundances, the heavy elements contribute to the total mass. This means that the hydrogen density and $S(\text{H}\beta)$ are lower for the same mass but higher Z. The surface brightness is highest for solar abundances, where more of the $4M_{sun}$ is H so the density is higher. The coefficients in Equations (2.27), (2.28) and (2.29) were evaluated for abundances intermediate between solar and Crab. The maximum expansion velocity also affects the surface brightness because this sets the outer radius that appears in the equations. A shell with a larger expansion velocity is more spread out, has lower density, and lower $S(\text{H}\beta)$.

With these assumptions the physical conditions in the outer shell, the ionization and temperature, can be computed. Observations described below suggest that the upper limit to Hβ is about $S(\text{H}\beta) < 4\times10^{-18}$ erg cm^{-2} s^{-1} arcsec^{-2}. If we apply

different values of m, indicating different abundances, into Equations (2.27), (2.28) and (29), we obtain that case I and case II have average surface brightness that are less than this observed limit for all abundances. Case III has a surface brightness that is under this observed limit for Crab abundances but above this observed limit for solar and ISM abundances. We consider all these models in the following to examine their predictions.

2.3 Model calculations

Here we will consider models with various compositions and power laws to compute the emitted spectrum. Case I and case II are more consistent with the existence of a large mass, $4M_{sun}$, and the limits to the surface brightness (Fesen, Shull & Hurford 1997; Tziamtzis et al. 2009). Since they have similar results for all kinds of calculations, we only give the full results for case I as examples. Sollerman et al. (2000) say that solar abundances might be most appropriate if the outer shell comes from the upper envelope of the star. We adopt this and further assume that grains have not formed in the fast wind. We present results for all the scenarios below, but will focus on this single model.

2.3.1 The emission-line spectrum

We use version 13 of the plasma simulation code Cloudy (Ferland et al. 2013) to predict the observed spectrum. We computed the luminosities of many emission lines and converted them to surface brightness by dividing the luminosities by the size derived above. We obtain different emission lines and surface brightness for the three different models. Figure 2.1 shows predicted spectra integrated over the full outer shell for case I with solar abundances. The upper panel shows the full range 0.1 to 100 microns. The lower panel shows the range 1 to 30 microns in greater detail. We focus on the UV – IR spectral region since this would be easiest to study with today's instrumentation.

Table 2.2 to Table 2.10 give the average surface brightnesses S for IR, optical and UV emission lines, as defined by Equation (2.27), (2.28) and (2.29), for models with different abundances. These can be compared to the best observational upper limit achieved to date for the outer shell, $S < 1.2 \times 10^{-17}$ erg cm^{-2} s^{-1} arcsec^{-2} using long-slit spectra to search for Hα (Fesen, Shull & Hurford 1997, but with their value corrected upwards by a factor of 3.4 to correct for the observed extinction; Tziamtzis et al. 2009). All lines at or brighter than that limit are italicized in Table 2.2 to Table 2.10.

Hα is brighter than the observational limit in case III with solar or ISM abundances, so at face value these models appear to be ruled out, at least for an outer shell containing the full amount of the missing mass. However, scattered light from the much brighter parts of the Crab is a major issue, as has been discussed by Tziamtzis et al. (2009). The Fesen, Shull & Hurford (1997) upper limit really corresponds to radii beyond about 0.3' from the bright edge of the main nebula (R_{in}), because their spectrum inside that radius is likely to be dominated by an unknown amount of scattered light. Figure 2.2 shows an example of the emissivity in three emission lines as a function of the depth into the shell from its inner edge at R_{in} for case I with solar abundances. Figure 2.3 shows the results of integrating these emissivities along the line of sight through the outer shell to find the predicted surface brightness as a function of R_{proj}/R_{in} for cases I, II and III. We used solar abundances and assumed a distance of 2 kpc and a spherical shell. Note that Figure 2.3 is shown with linear scales for both radius and surface brightness, to make the wide range in surface brightness more obvious, and that each panel has been separately scaled in surface brightness. Each panel also shows the Fesen, Shull & Hurford (1997) Hα upper limit as a horizontal line beginning at a point 0.3' beyond $R_{in.}$ The lack of an Hα detection does nothing to rule out cases I or II, nor does it firmly rule out case III. Further ground-based observations might be able to push these optical-passband limits slightly fainter, but observations in Hα or other lines that are also emitted by the main part of the nebula will require great attention to the scattered light issue.

What is needed are unique spectroscopic tracers in the form of high-ionization lines not emitted by the filaments or (hopefully) by the thin [O III]-emitting skin (Sankrit & Hester 1997) that surrounds the outer edge of the synchrotron bubble. Our models predict strong emission lines from high-ionization species of C, N, O, Ne, Si, Mg and Fe, principally in the UV and IR parts of the spectrum. A surface brightness limit similar to that for Hα might be reachable in a few UV lines, notably C IV $\lambda\lambda$1548,1551, in about 3 hrs of on-target exposure (plus an equal sky exposure) using Hubble Space Telescope Advanced Camera for Surveys (ACS) imaging with very heavy on-detector binning. But the most promising lines are in the mid-IR, particularly [Ne VI] λ7.652μm which is also shown on Figure 2.3. Although these IR lines are somewhat fainter than the UV lines, they could be targeted with either SOFIA or (eventually) JWST mid-IR imagers and spectrographs. Archival Spitzer images and long-slit spectra also exist, and might be worth co-adding to search for these lines. Firm statements could be made about cases II or III if an IR measurement as deep as the Hα limit could be obtained.

An alternative to searching areas off to the side of the main part of the Crab would be to obtain spectra averaging over a fairly large area at the center of the Crab where the projected expansion velocities are towards and away from us, and searching for these mid-IR lines with positive and negative velocity shifts corresponding to the shell structure. Lundqvist & Tziamtzis (2012) used this method in the optical passband to search for [O III] and Ca II lines. The [Ne VI] 7.652μm line falls within the spectral range covered by the Spitzer IRS, but Temim et al. (2012) do not report any strong feature at this wavelength in their IRS spectra of the Crab. The predicted spectral signature for such emission lines would be two broad peaks displaced symmetrically around the Crab's heliocentric systemic velocity of about 0 km s^{-1} and separated by about 4000 km s^{-1}. We are in the process of carrying out the very careful reanalysis of the Spitzer spectra needed to search for faint features of this type. However, the low velocity resolution (4700 km s^{-1}) may prevent a clear distinction between any emission from an outer shell and

emission from the ionized outer skin of the main part of the Crab (see Lundqvist & Tziamtzis 2012, their figure 9).

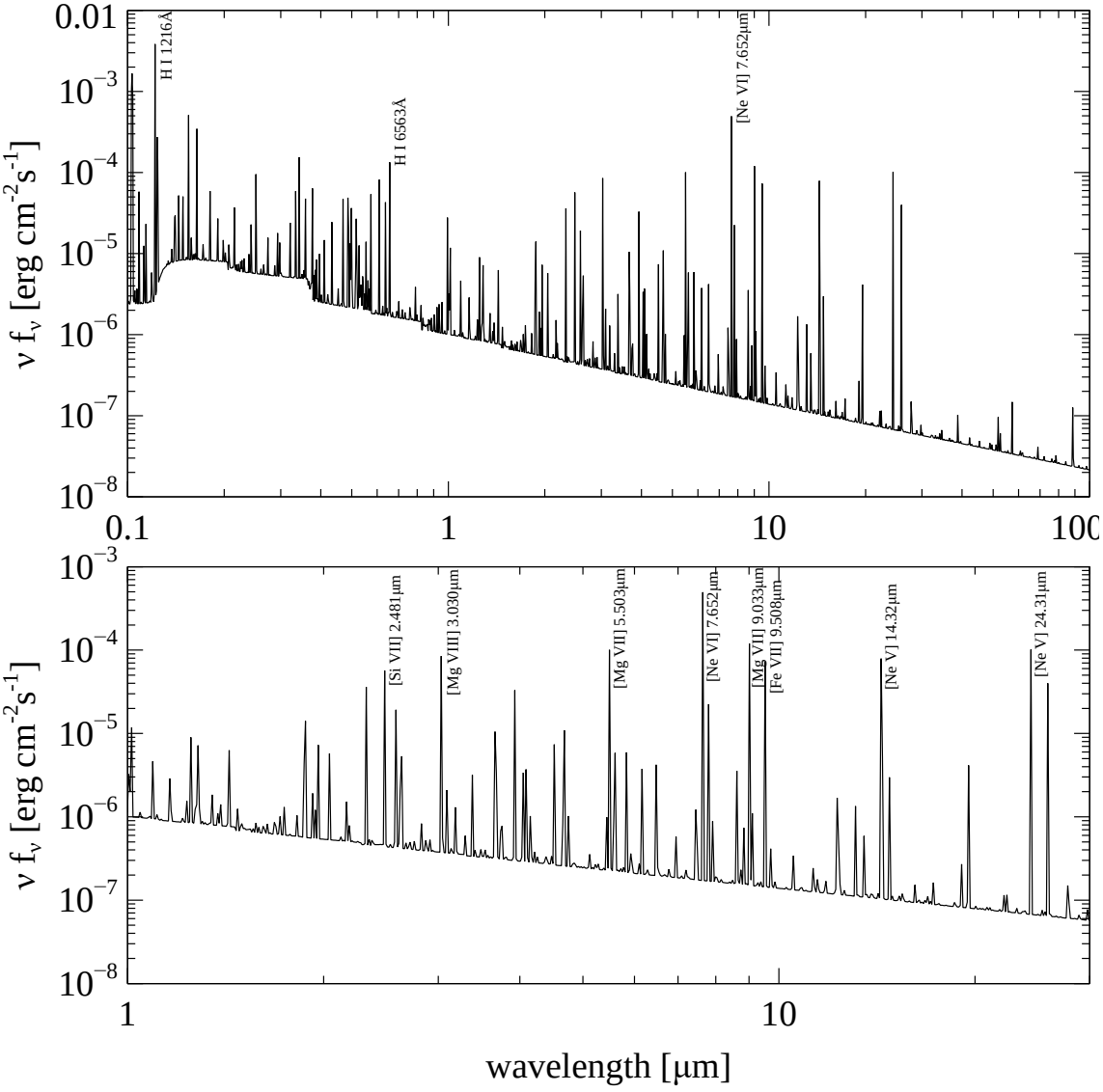

Figure 2.1 The upper panel shows emission lines from Crab outer shell between the wavelength of 0.1μm and 100 μm for case I with solar abundances. H I 1216Å, H I 6563Å and [Ne VI] 7.652 μm are the strongest lines in UV, optical and IR bands respectively. The lower panel shows the emission lines for the same model in the range between 1 μm and 30 μm and all the lines that are brighter than Hβ line are marked on the figure.

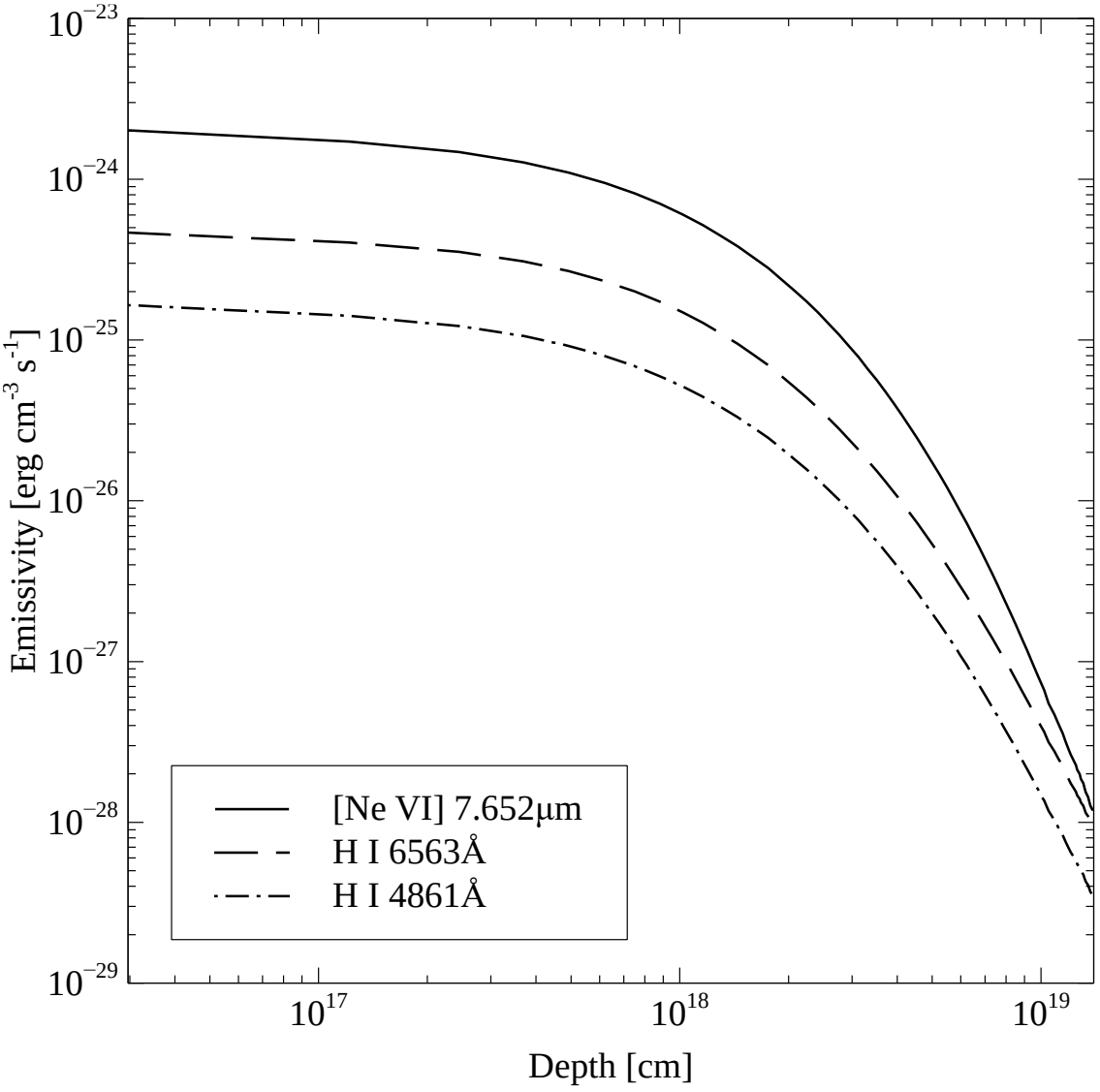

Figure 2.2 Emissivity as a function of depth of lines [Ne VI] 7.652 μm, H I 6563Å and H I 4861Å, for case I with solar abundances. For a distance of 2kpc, 2×10^{18} cm corresponds to 1.1'.

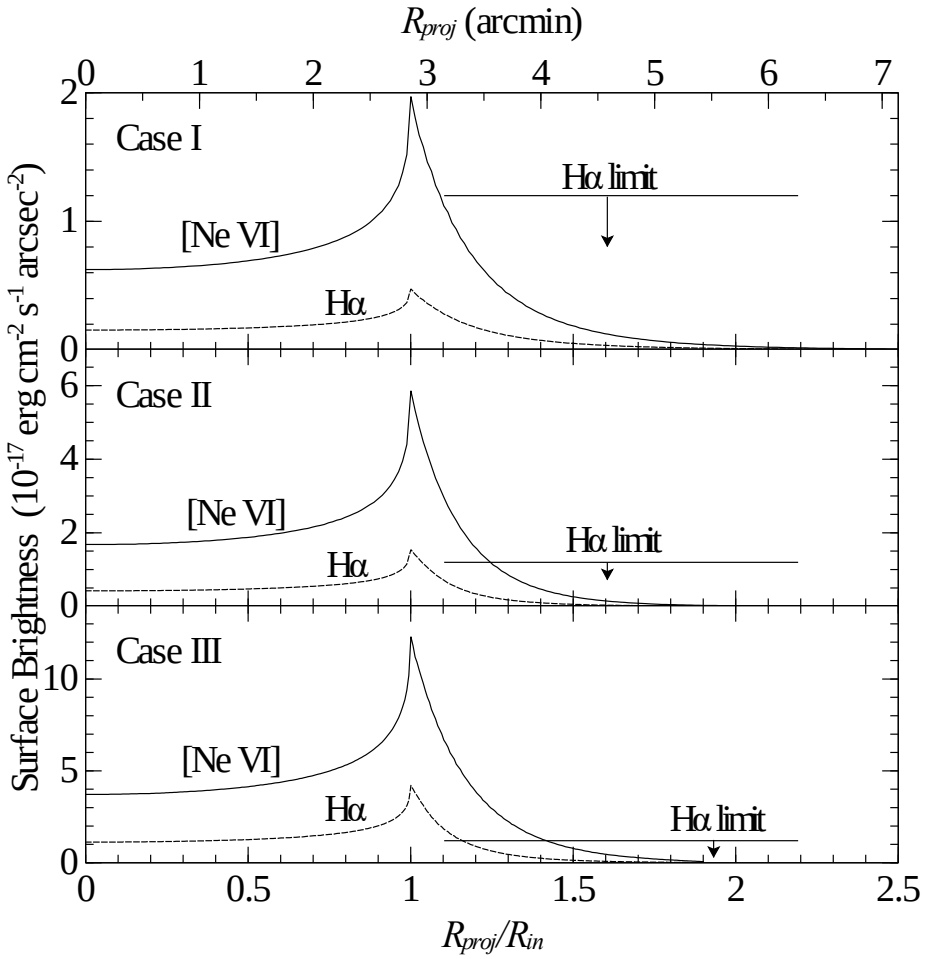

Figure 2.3 Predicted surface brightness of the [Ne VI] λ7.652μm and Hα emission lines, as a function of R_{proj}, the radial distance from the center of expansion as seen projected on the sky. These are computed for Cases I, II and III with solar abundances and assuming a distance of 2 kpc and a spherical outer shell of inner radius R_{in}=5×10^{18} cm. The surface brightness for R_{proj} <R_{in} includes both the front and rear sides of the outer shell. The horizontal bar in each panel shows the Fesen, Shull & Hurford (1997) Hα upper limit discussed in the text, starting at a point 0.3' beyond R_{in} and extending to the end of their slit.

Cloudy predicts the intensity of H I lines including line optical depths effect, collisional excitation and de-excitation, and continuum fluorescent excitation. The predicted H I intensities can be compared with Case B (pure recombination in which

Lyman lines are optically thick) and Case A (Lyman lines are optically thin and there is no continuum fluorescent excitation).

Table 2.11 compares H I luminosities for the solar abundance, case I Crab shell. It gives the computed luminosities with all processes included, along with the luminosities obtained from the computed density and temperature and assuming Case A and Case B emission (Storey & Hummer 1995). The predicted lines are about 10%~140% brighter than Case B, an indication that continuum fluorescent excitation is important. The Lyman lines in the outer shell are not optically thick so continuum pumping is important, causing them to be brighter than would be found with pure recombination. The optical depth in L$y\beta$, for instance, is about 1, so neither Case A nor Case B formally apply. The predicted deviations are not large and Case B is, as is often the case, a fair approximation to the actual emission.

2.3.2 Gas Temperature

Figure 2.4 shows the gas kinetic temperature across the outer shell. It increases as the depth increases for all three models. This is because the Crab radiation field, which powers the outer shell, decreases at r^{-2}, because of the inverse square law. The gas density falls off faster, as r^{-3} or r^{-4}. As a result, the ionization parameter, the ratio of photon to hydrogen densities (Osterbrock & Ferland 2006), increases as *r* increases. Higher ionization parameter gas tends to be hotter.

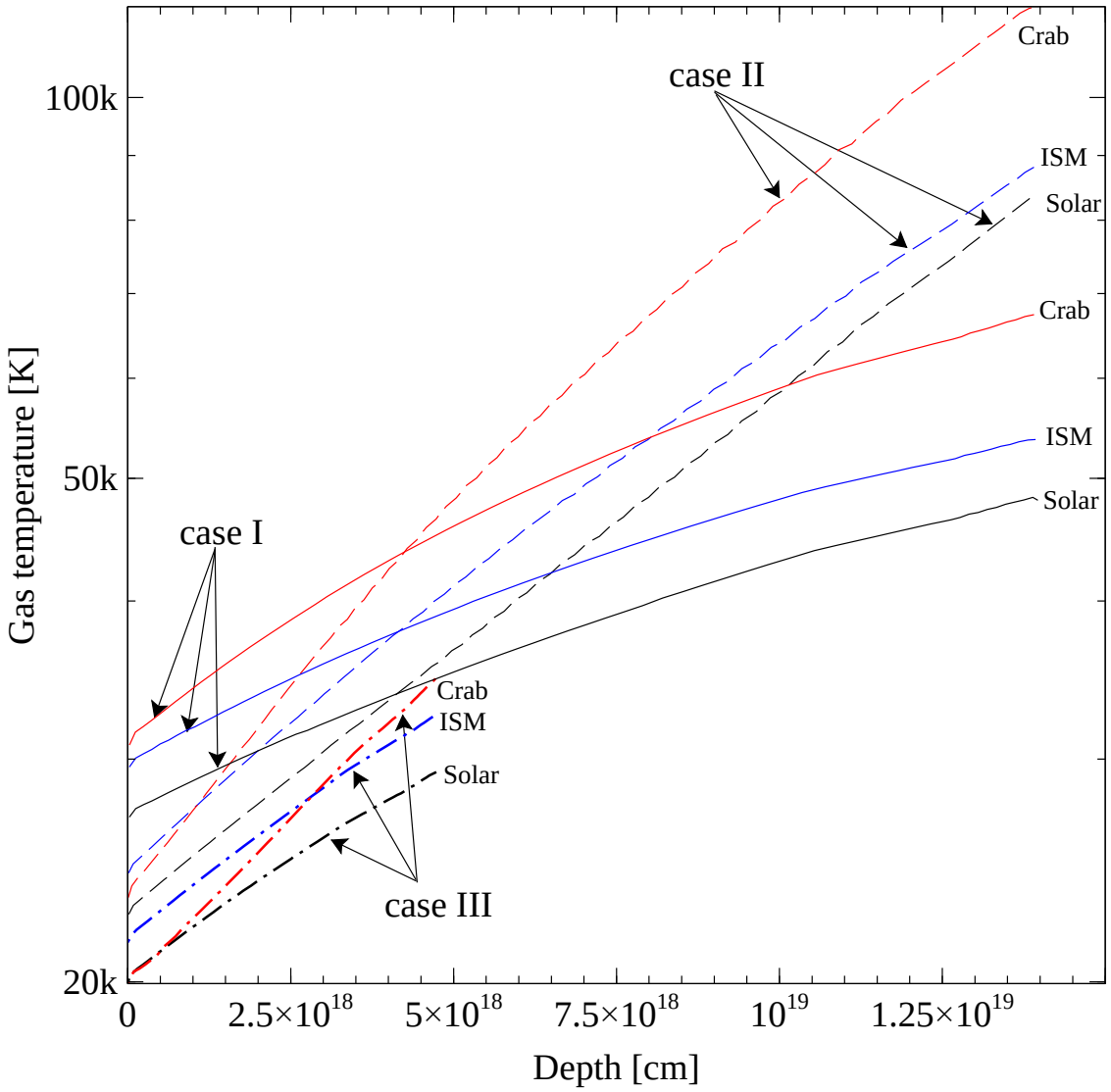

Figure 2.4 Gas temperature across the Crab outer shell for all the models. The depth is the distance between the illuminated face of the outer shell and a point within the outer shell.

2.3.3 The absorption line spectrum

We compute optical depths for different assumptions about the expansion velocities. Table 2.12 to Table 2.14 give the optical depths for models with Crab abundances, solar abundances and ISM abundances respectively. We continue to focus on the models with solar abundances. From Table 2.12 to Table 2.14 we see

that the optical depths for C IV 1549 doublet are not much greater than 1. The lines mainly form over a small radius due to the density decline, so the wind acceleration should not be large over the line forming region.

We make two assumptions to estimate the optical depth. First we assume a static shell. The lines are only thermally broadened. This would apply if there is no acceleration across the layer where the lines form. In this case there is sufficient opacity to produce the observed lines. In particular, the C IV 1549 doublet has an optical depth of 2.68, consistent with the Sollerman et al. (2000) tentative detection. We note that the optical depth of the O VI 1034 doublet is much larger than 1, which indicates strong absorption at that wavelength.

If the lines have a significant component of turbulence or if the expansion velocity changes across the line-forming region then the lines will be spread over a wider velocity range. Here the lines are optically thin.

Table 2.15 gives the computed line optical depths for both static and dynamic cases. We find the optical depth to be very small if we add a turbulence with velocity v =1680 km s^{-1} as the expansion velocity of the inner radius of the outer shell. The O VI 1034 doublet becomes optically thin as well.

The truth will lie between these two limiting assumptions. We will consider dynamic models, in which the velocity is determined self consistently, in future papers.

2.3.4 Is steady state appropriate?

2.3.4.1 Recombination time scale

The recombination time scale is defined as (Osterbrock & Ferland 2006)

$$t_{rec} = \frac{1}{n_e \alpha_{\mathrm{B}}(T_e)} \tag{2.30}$$

where n_e is the electron density and $\alpha_{\mathrm{B}}(T_e)$ is the Case B recombination coefficient at temperature T_e. The gas in the outer shell is photoionized by light from the visible Crab. Since Cloudy supposes that the gas atomic processes that are responsible for thermal and ionization equilibrium have reached steady state, we need to compare the age of the Crab with the recombination time to see if this is valid. We compute the recombination timescale for $Ne^{+6} \rightarrow Ne^{+5}$ for all three cases with solar abundances. We focus on this ion since it produces the strongest IR line. Since the temperature increases very slowly but the electron density decreases very quickly, we assume different radii have roughly the same recombination coefficient and evaluate it from the Badnell (2006), Badnell et al. (2003) and Badnell web site (http://amdpp.phys.strath.ac.uk/tamoc/DR/). We find the recombination time are about 100 years, 20 years and 10 years in the inner edge of the shell for the case I, case II and case III respectively (Figure 2.5). All of these are much shorter than the age of the visible Crab, suggesting that the outer shell has reached photoionization equilibrium.

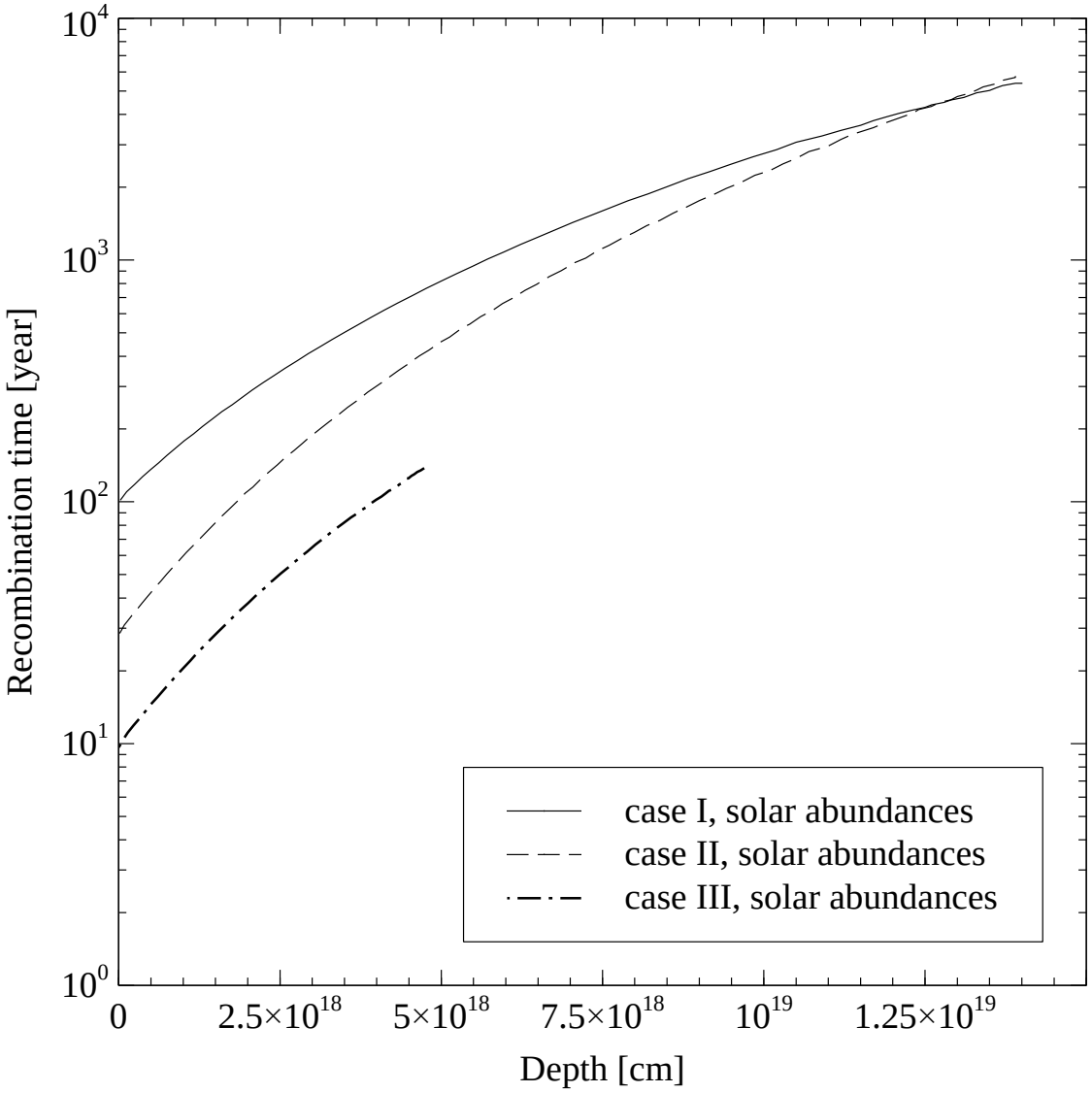

Figure 2.5 Recombination time scales for producing Ne^{+5} as a function of depth in the Crab outer shell for all three cases with solar abundances.

2.3.4.2 Thermal timescale

We calculate both the thermal energy [erg cm^{-3}] and the cooling rate [erg $cm^{-3}s^{-1}$] as a function of the radius for all three cases with solar abundances. From the ratio we can find the cooling time. We also calculate the emission measure for different radii or different zones. The differential emission measure for each depth is then

$$\mathrm{d}EM = 4\pi r^2 n(r)^2 dr. \quad (2.31)$$

This gives an indication of which portions of the shell contribute most to the observed emission.

Figure 2.6 shows the cooling times and the differential emission measure across the Crab outer shell for all three cases with solar abundances. We find the cooling time for all cases to be much longer than the age of the visible Crab. Even for the inner edge, which produces much of the emission measure, the cooling times are still about 20, 10 and 6 times of the age of the visible Crab for case I, case II and case III respectively. This indicates that the outer shell has not had time to reach thermal equilibrium, so retains a memory of its temperature in the past.

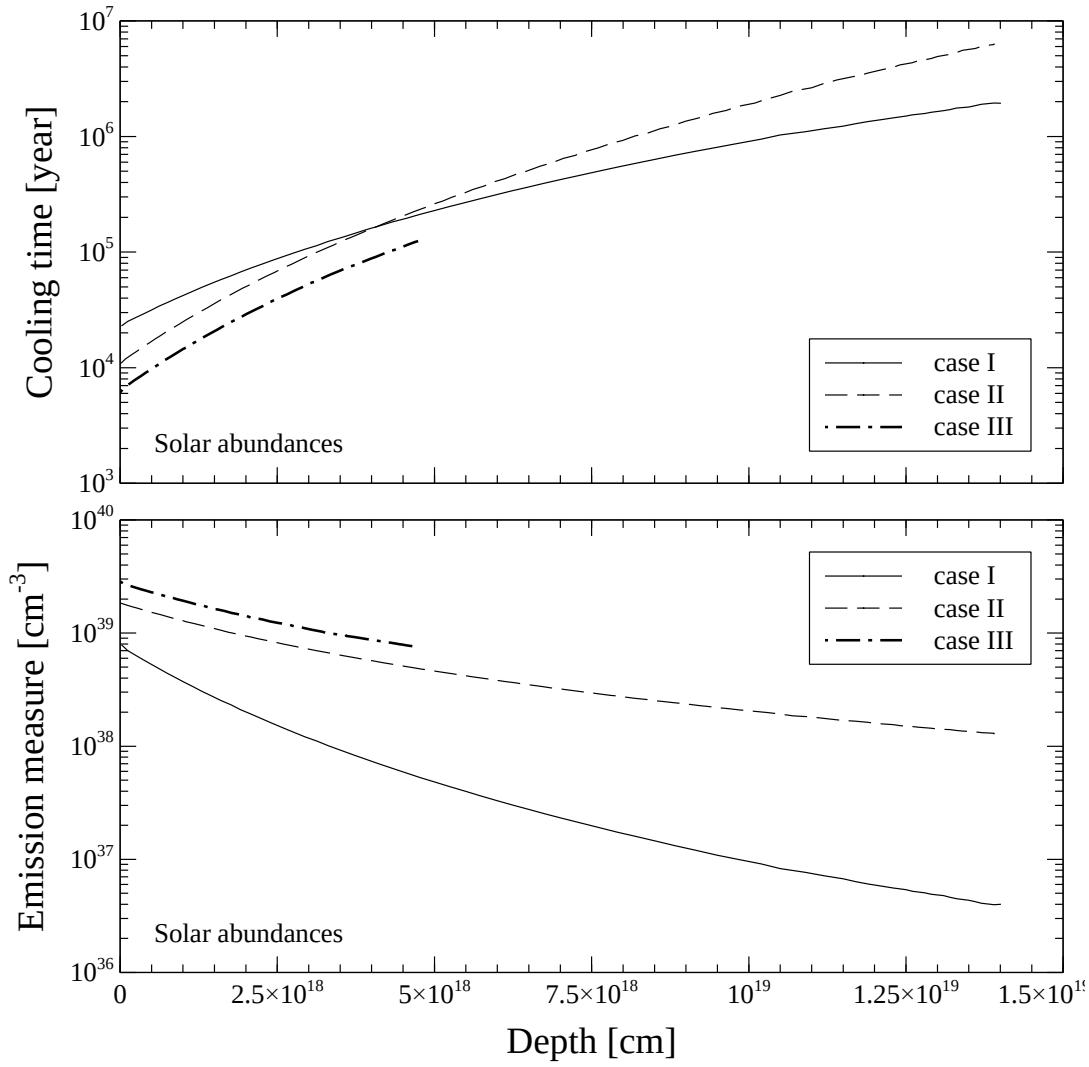

Figure 2.6 Cooling times and differential emission measures for all three cases with solar abundances. The innermost regions have the greatest emission measure and so would contribute the most to the observed spectrum.

2.3.4.3 Effects on predicted spectrum

The shell is in photoionization, but is not in thermal, equilibrium. This means that atomic processes which set the ionization of the gas have reached steady state, and that the predicted ionization should be accurate. The fact that the gas is not in thermal equilibrium means that we don't really know its temperature, only that it is

young enough to "remember" its temperature long ago. In other words, the current temperature is partially determined by its temperature in the past. We don't know whether the outer shell was initially hot or cold.

All of this is important because we predict that high ionization IR lines should be among the strongest lines in the optical-IR spectrum. Are these predictions approximately valid?

The uncertain temperature should not greatly affect the high ionization lines in the IR. The emissivities of an IR collisionally excited line do not have a strong temperature dependence. The lines have low excitation potentials, their Boltzmann factors should be close to unity, so their emissivity is proportional to $T^{-\frac{1}{2}}$ (Osterbrock & Ferland 2006). The optical recombination lines have an emissivity that is a faster power law, typically $T^{-0.8}$. Factors of two uncertainties in the temperature carry over to uncertainties in the line's surface brightness by well less than a factor of two.

Similarly, the uncertain temperature should not greatly affect the predicted ionization of the gas. The ionization is set by the photoionization and recombination rates. The photoionization rate has no temperature dependence, while recombination coefficients have power-law temperature dependencies, roughly $T^{-0.8}$. Factors of two uncertainties in the temperature will change the ionization by less than this.

Lundqvist, Fransson, & Chevalier (1986) gave time-dependent numerical simulations. We do have the ability to do time dependent, fully advective, photoionization flows (Henney et al. 2005; 2007). However, these calculations would have to be guided by observations that do not now exist. Is the shell cooling down from a hotter phase, warming up from a colder phase, or is it now in approximate thermal equilibrium?

2.4 Discussion and conclusions

We have presented a series of photoionization equilibrium calculations of the properties of the outer shell in the Crab Nebula. We reach the following conclusions.

- The gas cooling time is far longer than age of visible Crab, so the outer shell is not in thermal equilibrium. As a result, we don't really know its temperature since it will carry a memory of its original value.
- The recombination time is much shorter than the age of the Crab, so the outer shell is in ionization equilibrium.
- Together these mean that the outer shell will be highly ionized but we are not certain of its temperature. We find that the IR coronal lines are very strong, stronger than most optical lines used in previous searches. Luckily, these lines are not sensitive to the gas temperature so this is a robust prediction.
- The outer shell can produce the observed C IV absorption if the line broadening across the line-forming region is not large. Full dynamical solutions would be needed to make robust predictions of this line optical depth.
- The existing observational limit on Hα does not place useful constraints on most of our models, but is on the verge of ruling out models with solar and ISM abundances and $\alpha < -4$, $v \propto r^2$ and containing the full amount of the missing mass.
- The IR coronal lines are our best hope for avoiding confusion with scattered light from the inner parts of the Crab. The species producing them are too highly ionized to be produced by the photoionized gas in the filaments, and are higher ionization than the shocked gas that directly produces the [O III] emission skin at the outer edge of the synchrotron bubble (although higher velocity shocks could co-exist in this latter region and produce such lines).
- We recommend imaging (or spectroscopy) on the sky just outside the main part of the Crab to search for one of these IR lines.

- An alternative approach would be to search for these lines in spectra of the center of the Crab where the projected expansion velocities are towards and away from us.

Table 2.1 Basic parameters of the outer shell for three difference cases

Case	γ	α	β	$n_0(\mathrm{cm}^{-3})$	$R_{out}(\mathrm{cm})$
I	1	-3	0	0.87	1.90E+19
II	1	-4	0	1.58	1.90E+19
III	2	-4	-1	2.46	9.50E+18

Table 2.2 Predicted IR emission line average surface brightness, sorted by surface brightness for each model, for all lines brighter than Hβ, for case I.

Crab Abund.		Solar Abund.		ISM Abund.	
Line[1]	Surf. Br.[2]	Line	Surf. Br.	Line	Surf. Br.
[Ne VI] 7.652m	*1E-17*	*[Ne VI] 7.652m*	*1E-17*	*[Ne VI] 7.652m*	*1E-17*
[Ne V] 24.31m	2E-18	[Mg VII] 9.033m	3E-18	[Ne V] 24.31m	3E-18
[Mg VIII] 3.030m	2E-18	[Ne V] 24.31m	3E-18	[Ne V] 14.32m	2E-18
[Mg VII] 9.033m	2E-18	[Mg VII] 5.503m	3E-18	[S VIII] 9914	1E-18
[Mg VII] 5.503m	2E-18	[Mg VIII] 3.030m	2E-18	[Mg VII] 9.033m	1E-18
[Ne V] 14.32m	2E-18	[Ne V] 14.32m	2E-18		
He II 1.012m	5E-19	[Fe VII] 9.508m	2E-18		
[O IV] 25.88m	5E-19	[Si VII] 2.481m	1E-18		
[Fe VII] 9.508m	4E-19				
[Si IX] 3.929m	4E-19				
[S VIII] 9914	3E-19				
[Si VII] 2.481m	3E-19				

[1] Wavelengths are given in Å unless noted with m = microns.

Table 2.2 (continued)

[2]Surface brightness, erg cm^{-2} s^{-1} $arcsec^{-2}$.

Italicized entries have predicted surface brightness at or above the current optical-passband detection limit.

Table 2.3 Predicted optical emission line average surface brightness, sorted by surface brightness for each model, for all lines brighter than Hβ, for case I.

Crab Abund.		Solar Abund.		ISM Abund.	
Line[1]	Surf. Br.[2]	Line	Surf. Br.	Line	Surf. Br.
He II 4686	2E-18	H I 6563	3E-18	H I 6563	3E-18
H I 6563	8E-19	Fe VII 6087	2E-18	H I 4861	1E-18
Fe X 6375	7E-19	Fe VII 5721	1E-18		
Fe VII 6087	5E-19	H I 4861	1E-18		
Fe VII 5721	3E-19				
H I 4861	3E-19				

[1] Wavelengths are given in Å unless noted with m = microns.

[2]Surface brightness, erg cm^{-2} s^{-1} arcsec^{-2}.

Italicized entries have predicted surface brightness at or above the current optical-passband detection limit.

Table 2.4 Predicted UV emission line average surface brightness, sorted by surface brightness for each model, for all lines brighter than Hβ, for case I.

Crab Abund.		solar Abund.		ISM Abund.	
Line[1]	Surf. Br.[2]	Line	Surf. Br.	Line	Surf. Br.
O VI 1032+1038	*1E-16*	*O VI 1032+1038*	*2E-16*	*H I 1216*	*9E-17*
C IV 1548+1551	*1E-16*	*H I 1216*	*9E-17*	*O VI 1032+1038*	*9E-17*
H I 1216	*4E-17*	*H I 1026*	*3E-17*	*C IV 1548+1551*	*3E-17*
He II 1640	*1E-17*	*C IV 1548+1551*	*2E-17*	*H I 1026*	*3E-17*
O V 1211+1218	*1E-17*	*N V 1239+1243*	*2E-17*	*N V 1239+1243*	*2E-17*
N V 1239+1243	*1E-17*	*O V 1211+1218*	*1E-17*	*O V 1211+1218*	*1E-17*
H I 1026	9E-18	He II 1640	9E-18	He II 1640	8E-18
He II 1215	5E-18	[Ne V] 3426	3E-18	[Ne V] 3426	4E-18
[Ne V] 3426	3E-18	He II 1215	3E-18	He II 1215	3E-18
He II 1085	2E-18	Mg VII 2569	2E-18	Ne V 3346	2E-18
C III] 1907+1910	2E-18	Fe VII 3759	2E-18	He II 1085	1E-18
Mg VII 2569	2E-18	He II 1085	1E-18		
He II 1025	1E-18	Ne V 3346	1E-18		

Table 2.4 (continued)

Ne V 3346	1E-18	[Mg VI] 1806	1E-18
C V 1312	1E-18		
He II 2050	1E-18		
[C V] 2271+2275	8E-19		
He II 3203	8E-19		
Ne V 1141	7E-19		
[Mg VI] 1806	7E-19		
Si VIII 1446	5E-19		
He II 2733	4E-19		
C VI 1240	4E-19		
Fe VII 3759	4E-19		
He II 3645	3E-19		
O IV 1405	3E-19		
[Fe VII] 3586	3E-19		

[1] Wavelengths are given in Å unless noted with m = microns.

[2]Surface brightness, erg cm^{-2} s^{-1} $arcsec^{-2}$.

Italicized entries have predicted surface brightness at or above the current optical-passband detection limit.

Table 2.5 Predicted IR emission line average surface brightness, sorted by surface brightness for each model, for all lines brighter than Hβ, for case II.

Crab Abund.		Solar Abund.		ISM Abund.	
Line[1]	Surf. Br.[2]	Line	Surf. Br.	Line	Surf. Br.
[Ne VI] 7.652m	*5E-17*	*[Ne VI] 7.652m*	*4E-17*	*[Ne VI] 7.652m*	*4E-17*
[Ne V] 24.31m	*1E-17*	*[Ne V] 24.31m*	*1E-17*	*[Ne V] 24.31m*	*2E-17*
[Ne V] 14.32m	*1E-17*	*[Ne V] 14.32m*	*1E-17*	*[Ne V] 14.32m*	*1E-17*
[O IV] 25.88m	5E-18	[O IV] 25.88m	9E-18	[O IV] 25.88m	5E-18
[Mg VII] 9.033m	4E-18	[Fe VII] 9.508m	7E-18		
[Mg VII] 5.503m	4E-18	[Mg VII] 9.033m	6E-18		
[Mg VIII] 3.030m	3E-18	[Mg VII] 5.503m	5E-18		
[Fe VII] 9.508m	2E-18	[Si VII] 2.481m	4E-18		
He II 1.012m	1E-18				
[Si VII] 2.481m	1E-18				
[S VIII] 9914	8E-19				

[1] Wavelengths are given in Å unless noted with m = microns.

[2]Surface brightness, erg cm^{-2} s^{-1} $arcsec^{-2}$.

Table 2.5 (continued)

Italicized entries have predicted surface brightness at or above the current optical-passband detection limit.

Table 2.6 Predicted optical emission line average surface brightness, sorted by surface brightness for each model, for all lines brighter than Hβ, for case II.

Crab Abund.		solar Abund.		ISM Abund.	
Line[1]	Surf. Br.[2]	Line	Surf. Br.	Line	Surf. Br.
He II 4686	6E-18	H I 6563	9E-18	H I 6563	9E-18
H I 6563	2E-18	Fe VII 6087	7E-18	H I 4861	3E-18
Fe VII 6087	2E-18	Fe VII 5721	4E-18		
Fe VII 5721	1E-18	H I 4861	3E-18		
H I 4861	8E-19				

[1] Wavelengths are given in Å unless noted with m = microns.

[2]Surface brightness, erg cm^{-2} s^{-1} $arcsec^{-2}$.

Italicized entries have predicted surface brightness at or above the current optical-passband detection limit.

Table 2.7 Predicted UV emission line average surface brightness, sorted by surface brightness for each model, for all lines brighter than Hβ, for case II.

Crab Abund.		Solar Abund.		ISM Abund.	
Line[1]	Surf. Br.[2]	Line	Surf. Br.	Line	Surf. Br.
C IV 1548+1551	3E-16	H I 1216	2E-16	H I 1216	2E-16
O VI 1032+1038	2E-16	O VI 1032+1038	1E-16	O VI 1032+1038	1E-16
H I 1216	8E-17	C IV 1548+1551	7E-17	C IV 1548+1551	8E-17
He II 1640	4E-17	N V 1239+1243	5E-17	N V 1239+1243	5E-17
O V 1211+1218	3E-17	H I 1026	5E-17	H I 1026	5E-17
N V 1239+1243	2E-17	O V 1211+1218	3E-17	O V 1211+1218	3E-17
H I 1026	2E-17	He II 1640	2E-17	He II 1640	2E-17
Ne V 3426	2E-17	Ne V 3426	1E-17	Ne V 3426	2E-17
He II 1215	1E-17	He II 1215	8E-18	He II 1215	8E-18
C III 1907+1910	1E-17	Ne V 3346	5E-18	Ne V 3346	6E-18
He II 1085	7E-18	Fe VII 3759	4E-18	He II 1085	4E-18
Ne V 3346	6E-18	He II 1085	4E-18		
HE II 1025	4E-18				
Mg VII 2569	3E-18				
He II 3203	3E-18				

Table 2.7 (continued)

C V 1312	2E-18
O IV 1401+1405	2E-18
Ne IV 2424	2E-18
Mg VI 1806	2E-18
Ne V 1141	2E-18
He II 2733	1E-18
Fe VII 3759	1E-18
C V 2275	1E-18
Fe VII 3586	9E-19
He II 2511	8E-19

[1] Wavelengths are given in Å unless noted with m = microns.

[2]Surface brightness, erg cm^{-2} s^{-1} $arcsec^{-2}$.

Italicized entries have predicted surface brightness at or above the current optical-passband detection limit.

Table 2.8 Predicted IR emission line average surface brightness, sorted by surface brightness for each model, for all lines brighter than Hβ, for case III.

Crab Abund.		Solar Abund.		ISM Abund.	
Line[1]	Surf. Br.[2]	Line	Surf. Br.	Line	Surf. Br.
[Ne VI] 7.652m	*1E-16*	*[Ne VI] 7.652m*	*8E-17*	*[Ne VI] 7.652m*	*1E-16*
[Ne V] 24.31m	*7E-17*	*[Ne V] 24.31m*	*5E-17*	*[Ne V] 24.31m*	*6E-17*
[Ne V] 14.32m	*5E-17*	*[O IV] 25.88m*	*5E-17*	*[Ne V] 14.32m*	*5E-17*
[O IV] 25.88m	*3E-17*	*[Ne V] 14.32m*	*4E-17*	*[O IV] 25.88m*	*3E-17*
[Mg VII] 9.033m	8E-18	*[Fe VII] 9.508m*	*2E-17*		
[Mg VII] 5.503m	7E-18	*[Mg VII] 9.033m*	*1E-17*		
[Fe VII] 9.508m	6E-18	*[Si VII] 2.481m*	*1E-17*		
[He II] 1.012m	4E-18				
[Mg VIII] 3.030m	3E-18				
[Si VII] 2.481m	3E-18				

[1] Wavelengths are given in Å unless noted with m = microns.

[2]Surface brightness, erg cm^{-2} s^{-1} $arcsec^{-2}$.

Italicized entries have predicted surface brightness at or above the current optical-passband detection limit.

Table 2.9 Predicted optical emission line average surface brightness, sorted by surface brightness for each model, for all lines brighter than Hβ, for case III.

Crab Abund.		Solar Abund.		ISM Abund.	
Line[1]	Surf. Br.[2]	Line	Surf. Br.	Line	Surf. Br.
He II 4686	*2E-17*	*H I 6563*	*2E-17*	*H I 6563*	*2E-17*
H I 6563	6E-18	*Fe VII 6087*	*2E-17*	*H I 4861*	*8E-18*
Fe VII 6087	5E-18	*Fe VII 5721*	*1E-17*		
Fe VII 5721	3E-18	H I 4861	9E-18		
H 1 4861	2E-18				

[1] Wavelengths are given in Å unless noted with m = microns.

[2]Surface brightness, erg cm^{-2} s^{-1} arcsec^{-2}.

Italicized entries have predicted surface brightness at or above the current optical-passband detection limit.

Table 2.10 Predicted UV emission line average surface brightness, sorted by surface brightness for each model, for all lines brighter than Hβ, for case III.

Crab Abund.		Solar Abund.		ISM Abund.	
Line[1]	Surf. Br.[2]	Line	Surf. Br.	Line	Surf. Br.
C IV 1548+1551	*9E-16*	*H I 1216*	*3E-16*	*H I 1216*	*3E-16*
O VI 1032+1038	*2E-16*	*C IV 1548+1551*	*2E-16*	*C IV 1548+1551*	*2E-16*
H I 1216	*1E-16*	*O VI 1032+1038*	*2E-16*	*O VI 1032+1038*	*1E-16*
He II 1640	*1E-16*	*N V 1239+1243*	*8E-17*	*N V 1239+1243*	*9E-17*
C III] 1907+1910	*5E-17*	*He II 1640*	*6E-17*	*H I 1026*	*6E-17*
[Ne V] 3426	*5E-17*	*H I 1026*	*6E-17*	*He II 1640*	*6E-17*
O V 1211+1218	*5E-17*	*O V 1211+1218*	*6E-17*	*[Ne V] 3426*	*5E-17*
He II 1215	*4E-17*	*[Ne V] 3426*	*4E-17*	*O V 1211+1218*	*5E-17*
N V 1239+1243	*4E-17*	*He II 1215*	*2E-17*	*He II 1215*	*2E-17*
H I 1026	*4E-17*	*Ne V 3346*	*1E-17*	*Ne V 3346*	*2E-17*
He II 1085	*2E-17*	*Fe VII 3759*	*1E-17*	*Ne IV 2424*	*1E-17*
Ne V 3346	*2E-17*	*He II 1085*	*1E-17*	*N IV 1485*	*1E-17*
He II 1025	*1E-17*	*Ne IV 2424*	*1E-17*	He II 1085	9E-18
Ne IV 2424	9E-18			C III] 1907	9E-18
He II 3203	7E-18				

Table 2.10 (continued)

He II 2050	7E-18
C V 1312	4E-18
He II 2733	4E-18
O IV 1405	4E-18
Mg VII 2569	3E-18
[Mg VI] 1806	3E-18
Fe VII 3759	3E-18
Ne V 1141	3E-18
O IV 1401	3E-18
Mg V 2855	3E-18
He II 2511	2E-18

[1] Wavelengths are given in Å unless noted with m = microns.

[2]Surface brightness, erg cm^{-2} s^{-1} $arcsec^{-2}$.

Italicized entries have predicted surface brightness at or above the current optical-passband detection limit.

Table 2.11 H I luminosities for different cases (case I, solar) [erg s^{-1}]

Line	Total	Case B	Case A
H I 6563Å	2.09E+32	1.75E+32	1.04E+32
H I 4861Å	7.31E+31	6.47E+31	4.02E+31
H I 1216Å	5.86E+33	2.37E+33	1.40E+33
H I 1.875μm	2.05E+31	1.68E+31	1.43E+31

Table 2.12 Predicted optical depth, sorted by wavelength for thermal-broadened model, for case I.

Crab Abund.		Solar Abund.		ISM Abund.	
Line[1]	Opt. Dpt.[2]	Line	Opt. Dpt.	Line	Opt. Dpt.
O I 1025	3.56E-01	O I 1025	1.62E+00	O I 1025	1.42E+00
H I 1025	4.05E-01	H I 1025	1.88E+00	H I 1025	1.63E+00
O VI 1031+1037	3.21E+01	O VI 1031+1037	3.81E+01	O VI 1031+1037	2.19E+01
H I 1215	2.53E+00	H I 1215	1.17E+01	H I 1215	1.02E+01
N V 1239+1243	1.03E+00	N V 1239+1243	3.54E+00	N V 1239+1243	2.88E+00
C IV 1548+1551	1.32E+01	C IV 1548+1551	2.68E+00	C IV 1548+1551	2.33E+00

[1] Wavelengths are given in Å.

[2]Optical Depth.

Table 2.13 Predicted optical depth, sorted by wavelength for thermal-broadened model, for case II.

Crab Abund.		Solar Abund.		ISM Abund.	
Line[1]	Opt. Dpt.[2]	Line	Opt. Dpt.	Line	Opt. Dpt.
H I 1025	1.16E+00	H I 1025	4.69E+00	H I 1025	4.17E+00
O I 1025	9.81E-01	O I 1025	3.92E+00	O I 1025	3.53E+00
O VI 1031+1037	6.78E+01	O VI 1031+1037	6.34E+01	O VI 1031+1037	3.75E+01
H I 1215	7.24E+00	H I 1215	2.93E+01	H I 1215	2.61E+01
N V 1239+1243	3.04E+00	N V 1239+1243	8.42E+00	N V 1239+1243	7.06E+00
C IV 1548+1551	5.50E+01	C IV 1548+1551	8.61E+00	C IV 1548+1551	7.79E+00

[1] Wavelengths are given in Å.

[2]Optical Depth.

Table 2.14 Predicted optical depth, sorted by wavelength for thermal-broadened model, for case III.

Crab Abund.		Solar Abund.		ISM Abund.	
Line[1]	Opt. Dpt.[2]	Line	Opt. Dpt.	Line	Opt. Dpt.
H I 1025	3.51E+00	H I 1025	1.31E+01	O I 1025	9.75E+00
O I 1025	2.86E+00	O I 1025	1.06E+01	H I 1025	1.18E+01
O VI 1031+1037	1.34E+02	O VI 1031+1037	1.03E+02	O VI 1031+1037	6.24E+01
H I 1215	2.19E+01	H I 1215	8.17E+01	H I 1215	7.37E+01
N V 1239+1243	8.35E+00	N V 1239+1243	1.99E+01	N V 1239+1243	1.71E+01
C IV 1548+1551	2.00E+02	Si IV 1394	1.47E-01	C IV 1548+1551	2.51E+01
		C IV 1548+1551	2.72E+01		

[1] Wavelengths are given in Å.

[2]Optical Depth.

Table 2.15 Line optical depths for static and dynamic cases (case I, solar)

Line	Thermal	v =1680 km s^{-1}
O VI 1031Å+1037Å	38.1	1.81E-01
C IV 1548Å+1551Å	2.68	1.95E-02

CHAPTER 3 Molecular hydrogen emission as a density and temperature indicator

3.1 Introduction

Recent observations in the 1-2 micron window have discovered that a variety of exotic objects have surprisingly strong H_2 emission relative to the infrared H I recombination lines. Some examples include knots in the Helix planetary nebula (O'Dell et al. 2005, 2007; Henney et al. 2007), the filaments surrounding brightest cluster galaxies in cool-core clusters (Jaffe, Bremer & van der Werf 2001; Johnstone et al. 2007; Ferland et al. 2009), and Crab Nebula filaments (Loh et al. 2010). In these objects the H_2 1-0 S(1) line is several dex brighter, relative to nearby H I lines, than is found in star forming regions such as Orion (see table 3 of Loh et al. 2012). The goal of this paper is to examine the correct interpretation of these regions, and how this differs from the usual interpretation of the H_2 spectrum of H II regions/PDRs. However, in this paper we are not trying to make complete complex models. We create the simplest possible models to show basic physical processes. In star forming regions, the H I lines form by recombination in the H II region that is produced by ionizing stellar photons. The H_2 lines are thought to form in predominantly atomic regions of the PDR by a radiative fluorescence process whereby stellar photons near 0.1 μm are absorbed by electronic transitions in H_2. These excitations produce either dissociation or decay back into the ground electronic configuration X (Tielens & Hollenbach 1985). The latter produces H_2 emission whose intensity relative to H I recombination lines is set by the number of ~0.1 μm photons relative to the number of photons capable of ionizing hydrogen. This ratio is set by the stellar SED (Ferland 2011; Loh et al. 2011).

The H_2 lines seen in the cool-core clusters of galaxies, PN, or the Crab Nebula filaments are far stronger relative to H I emission than is seen in a PDR near an H II region. There are two questions – how is the warm gas produced, and what process produces the strong H_2 lines? The usual energy source offered in such situations is shock heating (recent models are given by Flower & Pineau Des Forêts 2010).

However, heating by dissipative MHD waves or by fast particles (Ferland et al. 2009) can also produce warm gas. Successful models of H_2 emission from the Helix (Henney et al. 2007), cool-core cluster filaments (Ferland et al. 2009), and Crab Nebula filaments (Richardson et al. 2013) show that H_2 emission is mainly collisionally excited within the warm gas, with photo and grain pumping being negligible.

Here we take a "back to basics" approach to try to understand in a model-independent way what the observations are really directly telling us about the conditions in the H_2 emitting region. The first step in understanding the H_2 lines is to account for their intensities relative to hydrogen recombination lines. The next in understanding the H_2 lines is to measure a sufficient number of H_2 lines to create the level population diagrams (often called "excitation diagrams"), which is the focus of this paper. If the density is high enough for the molecule to be in LTE then the level excitation temperature will equal the gas kinetic temperature and H_2 lines can be used to measure the amount of molecular material. However there is no direct way to measure the density of the H_2 region and we are limited to level population diagrams. How do the H_2 level population diagrams change when the LTE assumption breaks down in the simplest case, where only thermal collisions are important? Could the diagram itself be used to determine the density from deviations from LTE, and whether the H_2 lines form in predominantly atomic or in predominately molecular gas?

In this paper we consider a unit cell of gas in which the hydrogen molecule is excited only by collisions with thermal particles. A variety of processes can, in principle, excite levels within H_2. These include grain formation pumping, fluorescent excitation, and cosmic ray or suprathermal particle excitation. We include many such processes in complete calculations, as described in Shaw et al. (2005) and Ferland et al. (2013). Some of these are very important for understanding the relatively faint H_2 lines seen in PDRs. However, they are unlikely to make significant contributions to the very strong lines we see in other environments, for the basic

reason that many of these processes produce emission while creating or destroying the molecule. The rate at which photons are produced is limited by these rates, which are often far slower than collisions with thermal particles. In the Helix and Crab Nebula filaments the shape of the SED means that fluorescent excitation is not significant (Henney et al. 2007; see figure 5 of Loh et al. 2012) and no sources of starlight are found in most of the cool-core cluster filaments (Ferland et al. 2009). The original motivation for this paper was a discussion of how to compute the "critical density", taken as an indication of whether level populations are close to their LTE value. Ferland et al. (2009) used the plasma physics community definition, the density where the collisional and radiative de-excitation rates are equal. This is quite different from the critical density used in the physical chemistry literature (Le Bourlot, Pineau des Forêts & Flower 1999). It has no rigorous definition, but the most useful purpose of the "critical density" is whether levels have a thermal population. The plasma literature uses a definition that is related to collisional and radiative de-excitation rates. We call this the "plasma critical density" but show that it does not describe anything useful in H_2. The most rigorous definition would be the density where all level populations are given by a Boltzmann population distribution. We call this the LTE critical density and show that it is surprisingly high. We find that there is also a very broad "quasi-thermal" density range where levels within a vibrational manifold have a thermal distribution but different manifolds do not continuously join onto one another.

The outline of this paper is as follows. In the next section we first show level populations predicted by complete PDR or shock calculations. These include many physical processes, but it is expected that fluorescent excitation and thermal collisions should be the dominant excitation process in these two cases. We then present simplified calculations, the focus of this paper, in which only thermal collisions excite the molecule. We show the level populations produced by thermal collisional excitation by a gas composed mainly of H^0 or mainly of H_2. We focus on a temperature of 2000 K, since this is produced by the selection effects described below, and is representative of the environments described above. Level population

diagrams are presented for a range of conditions, and we identify several diagnostics that could indicate the density, temperature, and chemical state. Finally we discuss implications of these calculations for diagnosing conditions in the H_2 regions of cool-core clusters of galaxies and the Crab Nebula.

3.2 Formalism and calculations

3.2.1 Complete models as reference cases

Much of the original literature on H_2 emission focused on complete models either of PDRs or of shocks. The models presented here are far simpler, so we begin by showing results of such complete calculations. Figure 3.1 shows the H_2 level population diagrams for a PDR model (left panel) calculated by version C13 of Cloudy, last described by Ferland et al. (2013) and two shock models (right panel). The PDR model is a modified version of the F1 model in Röllig et al. (2007) except that we used a density of 10^4 cm^{-3} to be similar to models considered below, and raised the radiation field intensity by 1 dex to keep the ratio of photons to baryons constant. The C and J shock models with the velocity of 20 km s^{-1} shown are similar to those in Flower & Pineau Des Forêts (2010), and newly recomputed using that code. A density of 10^4 cm^{-3} was chosen to allow comparison with the calculations shown below.

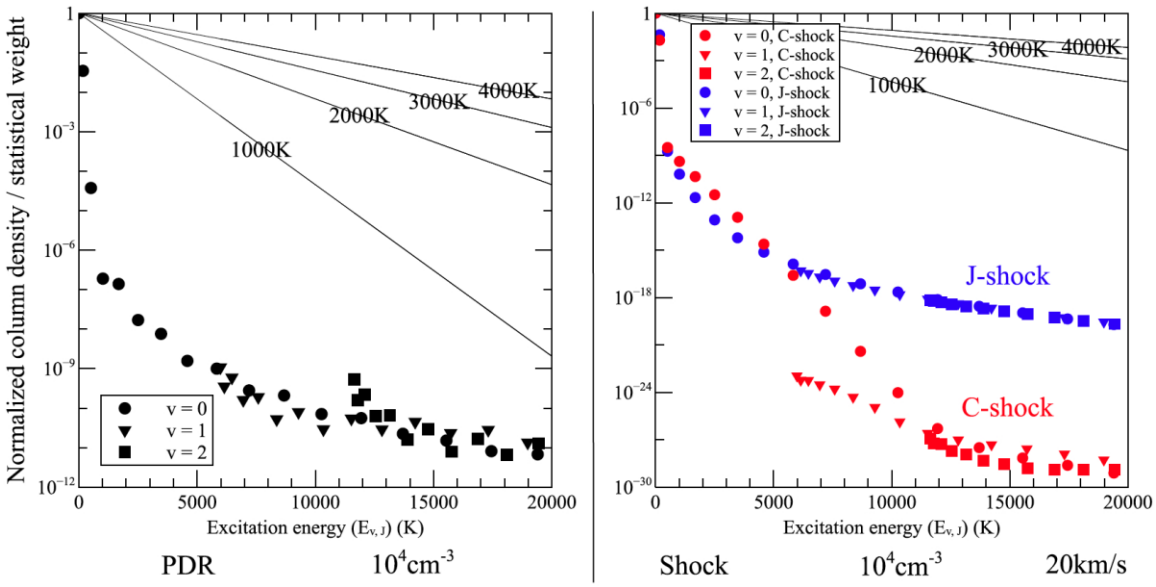

Figure 3.1 The left panel shows the H_2 level population diagram for a Leiden F1 PDR model with a hydrogen density of 10^4 cm^{-3}; the right panel shows the H_2 level population diagram for C and J shock models with the same hydrogen density and a velocity of 20 km s^{-1}.

3.2.2 Simplified calculations

The previous calculations of complete PDR and shock models include a large number of possible excitation processes and physical conditions. One purpose of this paper is to consider the H_2 emission properties and level populations of objects with very bright H_2 lines. To do this we set up calculations of gas with a single density and temperature. The excitation is only due to thermal collisions, which makes it possible to isolate the effects of density.

The H_2 model is described in Shaw et al. (2005) and Ferland et al. (2009). Rates for non-reactive collisions with H^0 come from Wrathmall, Gusdorf & Flower (2007) while those for H_2 are from Le Bourlot et al. (1999). Reactive H^0 exchange collisional rates are taken from Sun & Dalgarno (1994). The collision rates for H^0-H_2 collisions are larger than those for H_2-H_2 collisions, so we will consider each separately below. Transition probabilities come from Wolniewicz et al. (1998).

Tests presented in Shaw et al. (2005) and Röllig et al. (2007) show that our predictions for H_2 emission in PDRs, when all processes are included, are in good agreement with those of the codes described by Black & van Dishoeck (1987), Draine & Bertoldi (1996), Sternberg & Neufeld (1999), and Le Bourlot et al. (1995).

A single gas kinetic temperature of 2000K, thought to be characteristic of the strong-lined environments described above, is considered for most of this discussion. This temperature could be produced by a number of different processes. Ferland et al. (2009) argue that ionizing particles produce warm H_2 in cool-core cluster filaments, Graham et al. (1990) suggest that particles or energetic photons are responsible in the Crab Nebula, and Henney et al. (2007) show that advective flow of molecular gas into ionized regions produces warm H_2 in the Helix planetary nebula. Shocks are another possibility (Flower & Pineau Des Forêts 2010). Although the basic energy source differs, the H_2 emission is mainly produced by thermal collisional excitation in each of these cases.

Our previous work shows that strong temperature selection effects tend to produce this temperature (Ferland et al. 2008; Ferland et al. 2009; Loh et al. 2010). The levels producing the 2 micron emission come from highly-excited levels, corresponding to ~7000 K. Gas much cooler than 2000 K cannot excite the levels, while gas much warmer than this will dissociate molecular hydrogen. We focus on temperatures around 2000 K because these selection effects make the emission peak there (Ferland et al. 2008, figure 3). The excitation temperatures derived from H_2 observations are indeed generally around this value.

It is helpful to consider a simple a two-level system in discussing basic physical processes. Neglecting background radiation (so that stimulated terms can be omitted), and considering only atomic and molecular hydrogen, the equation of statistical equilibrium is

$$n_u\{A_{ul} + [n(\mathrm{H}^0)q_{ul}(\mathrm{H}^0) + n(\mathrm{H}_2)q_{ul}(\mathrm{H}_2)]\}$$

$$= n_l[n(\mathrm{H}^0)q_{lu}(\mathrm{H}^0) + n(\mathrm{H}_2)q_{lu}(\mathrm{H}_2)] \quad (3.1)$$

where n_u and n_l are the upper and lower levels of the H_2, $n(\mathrm{H}^0)$ and $n(\mathrm{H}_2)$ are the atomic hydrogen and molecular hydrogen as colliders respectively, and q_{ul} and q_{lu} are the collisional de-excitation rate coefficient and collisional excitation rate coefficient respectively. The solution to Equation (3.1) depends on the relative amounts of atomic and molecular hydrogen.

We consider two cases – the first where atomic collisions determine the level populations, and a second where molecular collisions dominate. As discussed below, atomic and molecular collisional rate coefficients have very different properties. We establish these limits by setting the $n(H_2)/n(H^0)$ fractions so that the dominant terms in the square brackets in Equation (3.1) are either $n(\mathrm{H}^0)q(\mathrm{H}^0)$ or $n(\mathrm{H}_2)q(\mathrm{H}_2)$. This results in level populations that are dominated by either the H^0 or H_2 collision rates.

Generally, for H^0 to dominate collisions, for the densities from 10^0 cm^{-3} to 10^8 cm^{-3}, $n(H^0)/n(H_2) > 3$ is required. Although this limit works well for the upper level of the H_2 1-0 S(1) line and the other commonly observed levels, is not applicable for the v=0 rotational levels which require $n(H^0)/n(H_2) > 10$ for the densities 10^0, 10^2, 10^4 cm^{-3}, and $n(H^0)/n(H_2) > 25$ for the densities 10^6 and 10^8 cm^{-3}. We focus on the H_2 1-0 S(1) line, the most commonly observed line, and the $n(H^0)/n(H_2) > 3$ limit is good enough for these lines. For the H_2-dominated case, considering the commonly observed levels, the $n(H^0)/n(H_2)$ limit depends on density. The ratio increases from $n(H^0)/n(H_2) < 5 \times 10^{-9}$ at the density 10^0 cm^{-3} to $n(H^0)/n(H_2) < 4.4 \times 10^{-3}$ at the density 10^8 cm^{-3}. All our models in this paper for the H_2-dominated collisions satisfied these conditions.

We changed the H^0/H_2 fraction by varying the grain catalysis formation rate to ensure that either the atomic or molecular collision rate (nq, with units s^{-1}) in Equation (3.1) dominates, indicating the atomic case or the molecular case mentioned in this paper. This is artificial and initially produced significant emission

due to grain formation pumping in some models. This process is normally treated assuming the excitation distribution functions given by Takahashi & Uehara (2001). To eliminate the spurious emission, we suppressed grain formation pumping by placing all newly-formed molecules in the J=0, 1 levels of v=0, with an ortho-para ratio of 3. Photo-excitation is effectively turned off by making the Balmer continuum quite faint. Galactic background cosmic rays are included but are set to a low density and have little effect. We tested and verified that either H^0 or H_2 collisions dominate the excitation for all levels in our multi-level models.

It may appear surprising that we are considering H_2 emission from atomic gas. Indeed, the H_2 density linearly affects the H_2 emissivity. However the most commonly observed H_2 lines, in the spectral region around 2 microns, come from levels with very high excitation energies, ~7000 K. The gas kinetic temperature affects the emission exponentially due to the Boltzmann factors. Predominantly atomic gas can produce strong H_2 emission if it is warm, as in the cool-core cluster models presented by Ferland et al. (2009) and the Crab Nebula models presented by Richardson et al. (2013). As discussed further below, and in Ferland et al. (2008) and Loh et al. (2010), the excitation and dissociation rates conspire to make H_2 most emissive at temperatures around 2000 K, where, in equilibrium, the gas will tend to be dominated by atomic collisions.

Finally, each calculation is a unit (1 cm^3) cell with a specified kinetic temperature and hydrogen density.

3.3 The plasma critical density

As defined for ions, in the graduate texts Draine (2011), Osterbrock & Ferland (2006), and Tielens (2005), the plasma critical density for upper level u is the density where the radiative and collisional de-excitation rates are equal. These texts give expressions similar to

$$n_{c,u} = \frac{\sum_{l<u} A_{ul}}{\sum_{l \neq u} q_{ul}}. \tag{3.2}$$

where A_{ul} is the radiative de-excitation rate from the upper level to the lower level and q_{ul} is the collisional de-excitation rate coefficient. The generalization to multi-level systems involves sums of decays to lower levels and the results depend on which levels are included.

As an illustration we show in Figure 3.2 the ratio of the sums given by Equation (3.2). For each level we formed the sum of the collisional rate coefficients or radiative rates down to all lower levels. We do not include any upward transitions, even for levels that are very close to each other. The collisional rate coefficients are shown for the atomic (left panel) and molecular (right panel) cases. The *v*=0, 1, and 2 manifolds are plotted as different symbols.

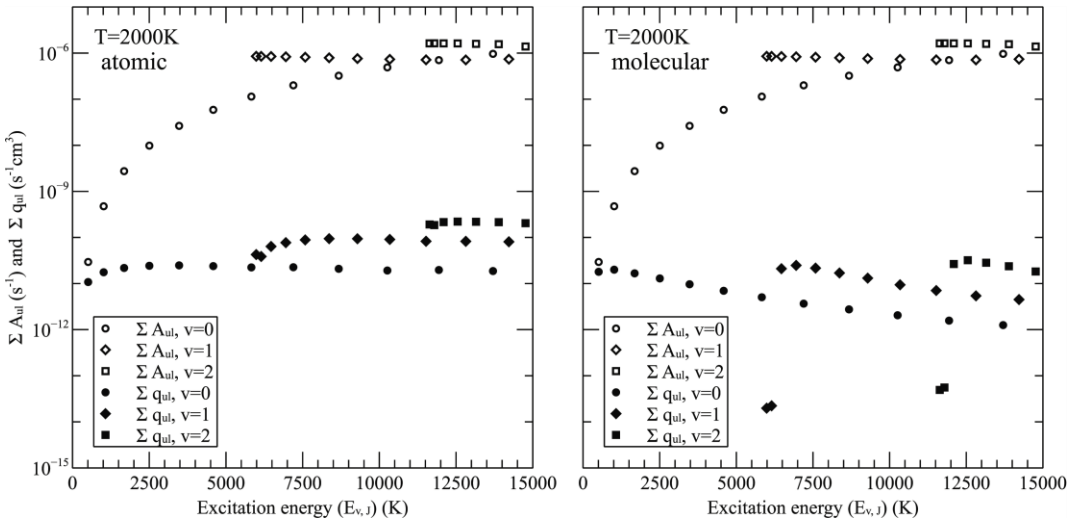

Figure 3.2 Radiative de-excitation rates and collisional de-excitation rate coefficients summed from upper energy levels having the excitation energy given as the independent axis to all possible lower levels. This is evaluated at *T*=2000K for the atomic case (left) and the molecular case (right).

The upper three sets of points in each panel show the sum of all radiative decays out of each level. These do not, of course, depend on the colliders, but are shown in both panels for convenience. The decay rate increases systematically with increasing *J* for

v=0, but has little dependence on J for v=1, 2. The decay rates increase with increasing v.

The lower three sets of points in the left panel of Fig. 3.2 give collisional de-excitation rate coefficients, which are the sum of all collisions from a given level to all lower levels, for the atomic case. There is only a modest systematic change in the collision rate as J increases along a v manifold, although the rate increases with increasing v. Proton exchange is possible with H^0 collisions, so these can induce ortho-para transitions, although such reactive collision rates are only available for the lower J in v=0.

The right panel shows similar data for the molecular case. The collisional de-excitation rate coefficients are usually dominated by the transitions in which the upper and lower levels have the same vibrational level but with J changing by 2 (see the online tables from Le Bourlot, Pineau des Forêts, & Flower 1999). The lowest J ortho and para level in each manifold have very small downward rates because they are the lowest levels in their vibrational manifolds, so there are no transitions to the lower rotational levels within the same vibrational levels. This shows that v-changing collisions are significantly less likely than J-changing collisions for molecular collisions. This is not true for the atomic case. The de-excitation rate coefficients for the lowest J level are the largest differences between the atomic and molecular cases. There is no tendency for the rates to change for different v.

The plasma critical density, the ratio given in Equation (3.2), is shown in Figure 3.3 for both the atomic and molecular cases. For both the atomic and molecular cases the plasma critical density in the v=0 manifold increases with increasing J because of the rapid increase in the radiative rates. There is no such trend in radiative rates for the v=1, 2 manifolds.

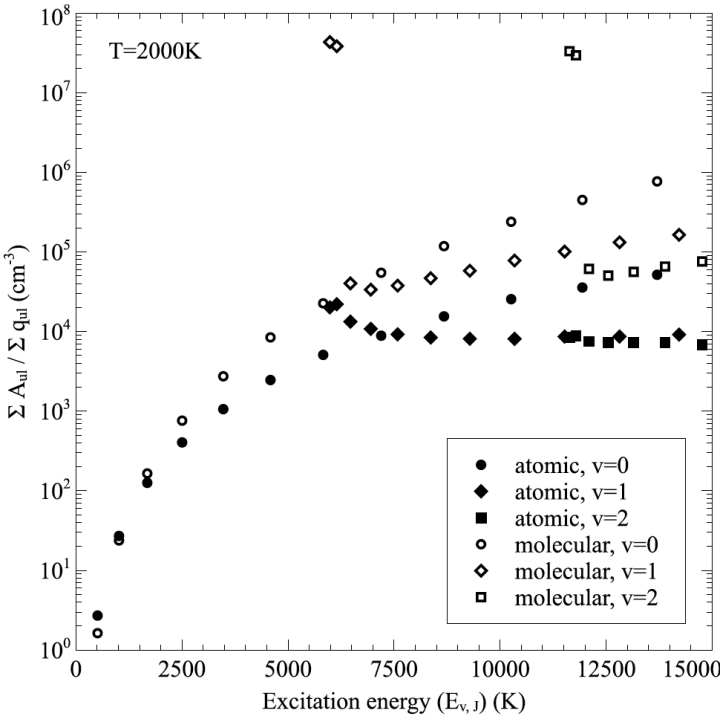

Figure 3.3 The ratio of the radiative rates to collisional de-excitation rate coefficients given by Equation (3.2). The sum is to all lower levels for the atomic and molecular cases at *T*=2000K. This is the simplest definition of a critical density.

The collisional rates for the atomic case are larger, often by about 1 dex, than the collisions for the molecular case. As a result the critical densities will be higher for a gas predominantly composed of H_2, and we expect that there will be larger deviations from LTE at moderate density.

Differences in the collisional rates for the atomic and molecular cases cause the differences seen in Fig. 3.3. For the atomic case the collisional de-excitation rate coefficient is smaller for *v*=0 than for *v*=1, 2, although the rates are similar for *v*=1 and 2. As a result the critical densities increase with *J* for *v*=0 but tend to be constant for *v*=1, 2. For the molecular case there is no systematic change in the rates for different *v* manifolds. Within each *v* manifold the collisional de-excitation rate coefficient decreases with increasing *J*, except for the lowest *J* levels for *v*=1, 2. This causes the plasma critical density to increase with *J* within a *v* manifold except the

lowest *J* levels. The very small downward rate from the lowest *J* in the vibrationally excited manifolds causes the plasma critical density of these levels shown in Fig. 3.3 to be very large in the molecular case.

In following sections we compare computed populations with their values in the LTE limit, to show whether the populations are thermal. We shall find that the situation is actually considerably more complicated than that shown in Fig. 3.3 and that the plasma critical density has little utility.

3.4 H_2 level populations

3.4.1 Level population diagrams

Level population diagrams are often used to determine excitation temperatures from measurements of H_2 line strengths. An observed intensity I is converted into a column density in the upper level, N_u, with

$$I = \frac{A_{ul} N_u h\nu_{ul}}{4\pi}. \tag{3.3}$$

These diagrams give the relationship between the excitation energy χ of the level and its column density N_u, divided by the statistical weight g. Figure 3.4 shows level population diagrams for all levels within 20 000K of ground, for both the atomic and molecular cases and for a number of different hydrogen densities. The column densities are normalized to the column density in the lowest level but have different scales for the atomic case and the molecular case because of the wide range in level population in the molecular case. The level populations were computed for a gas kinetic temperature of 2000K. For reference, solid lines give the LTE distribution at 2000K and at various other temperatures.

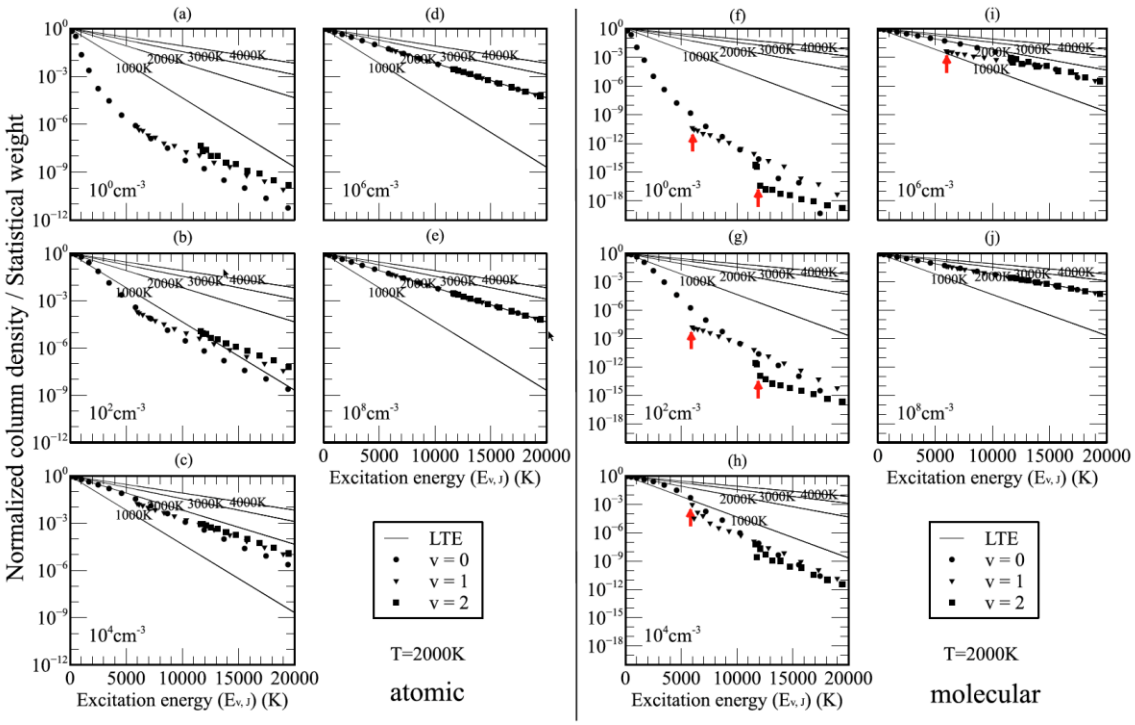

Figure 3.4 Level population diagrams for all levels within 20 000K of ground for the atomic (left) and molecular (right) cases at a gas kinetic temperature of T=2000K and the different hydrogen densities shown in each panel. The text refers to each panel by the letter given above it. The arrows point to the jumps between different vibrational manifolds as well as between different ro-vibrational levels for the molecular case.

The results are, at first sight, surprising. For both the atomic and molecular cases in the lowest J levels in v=0 at low densities the excitation temperature is lower than the kinetic temperature. For the atomic case the excited vibrational manifolds produce level population diagrams that look something like a Boltzmann distribution at the correct temperature, even at the lowest densities shown. For the molecular case a low-density gas produces larger deviations from a Boltzmann distribution than for the atomic case, and there are large jumps between v=0 and 1 manifolds, and between the lowest two levels of v=2 and the other higher J levels of the same vibrational manifold, due to the smaller molecular collision rates.

Consider Figure 3.4(a) and Figure 3.4(f), which are for hydrogen density of 10^0 cm^{-3}. This density is so far below the critical densities of any of the levels that the populations are close to the low-density limit and collisional de-excitation must be much slower than radiative decays and can be neglected. For such low densities, the slope and the derived excitation temperature of the v=0 manifold depends on the excitation energy, as was noted by Le Bourlot, Pineau des Forêts, & Flower (1999). For Fig. 3.4(a) and (f), the v=1, 2 manifolds fall roughly along straight lines which have slopes close to that of the 2000K LTE line and we will discuss this in §4.3.

The most striking aspect of the low-density diagrams shown in Fig. 3.4(a) and (f) is how much they resemble the non-thermal populations that are produced by fluorescent excitation or shocks (Fig. 3.1). This shows how difficult it is to determine the excitation physics from level populations alone.

Comparing Fig. 3.4 with Fig. 3.1, we find that the PDR calculation is very similar to the atomic case. In fact, most H_2 excitation in the PDR model occurs in regions that are predominantly atomic. Populations of lower levels are determined by collisional processes (van Dishoeck 2004) so their population distribution will be similar to the atomic case. The C-shock model's level population diagram is quite similar to the molecular case, and its line emission also originates in molecular regions. In contrast, The J-shock model produces a level population diagram that is similar to the atomic case. Here various levels are mainly populated in regions with different conditions. The lines from higher vibrational excited levels form in warmer atomic gas while the low-lying rotational levels form in cooler gas that is predominantly molecular.

3.4.2 The effects of density on level population diagrams

For the molecular case, the level populations in the v=0 and v=1 manifolds do not join smoothly together at low densities. There are also discontinuities between the levels v=2, J=0, 1, and the other higher J levels of the same v manifold. At low

densities the population is proportional to the ratio of collisional excitation to radiative de-excitation rates, which are shown in Fig. 3.2 and Fig. 3.3. The discontinuous jumps in the population are produced by the jumps in both rates and could be used as a density diagnostic. For instance, at a density of 10^2 cm^{-3} (Fig. 3.4(g)) the populations of levels from the v=0 and 1 manifolds are separated by factors of roughly 2 dex. At the same density, the levels from v=2, J=0, 1 and v=2, J=2 are separated by a factor of 1 dex. Such jump also exists at the density of 10^6 cm^{-3}. The amount of this separation depends on density, as shown, and this behavior could provide a density diagnostic. Since this discontinuous behavior only exists in the molecular case, not the atomic case, it could be used as a molecular region diagnostic. Although, for example, Fig. 3.4(b) and Fig. 3.4(g) have some similarity, if all the v=0, 1, 2 levels can be detected, we can tell the atomic and molecular cases apart. If only some v, J levels are detected, we will not be able to do so.

At the lowest densities the populations of excited vibrational manifolds are about 5 dex (Fig. 3.4(a)) and 10 dex (Fig. 3.4(f)) below the LTE limit for the atomic case and molecular case respectively. Lines from excited levels with higher v and higher J values would be very faint and hard to observe, especially for the molecular case, due to the low populations. The visibility increases with increasing density because the populations increase. This is a different way of seeing the density selection effect described by Ferland et al. (2008) and Loh et al. (2010).

At high densities the levels shown come into LTE, as expected. This occurs at a density of $\sim 10^6$ cm^{-3} for the atomic case and $\sim 10^8$ cm^{-3} for the molecular case. The different densities are due to the different collisional rates, with the molecular case having smaller rates and so requiring a higher density. The density where the levels come into LTE is another possible way to define a "critical density" for H_2. For the atomic case these densities are roughly one order of magnitude higher than the plasma critical densities suggested by Fig. 3.3, while for the molecular cases they are 2-3 orders of magnitude higher.

3.4.3 Quasi-thermal distributions along a vibrational manifold

For the T=2000K kinetic temperature used in most of our simulations, even at the very lowest density the v=1, 2 manifolds roughly fall along straight lines on level population diagrams such as Fig. 3.4. We will call this "quasi-thermal" behavior, because in the absence of further information such as observations of the v=0 points, it might be interpreted to mean that the emission comes from gas that is in LTE so the gas has high density. In Fig. 3.4 the v=1, 2 manifolds for the lowest-density atomic case fall along lines whose slopes correspond to a temperature about 200-300K below the actual kinetic temperature (panel a). For the molecular case the levels of v=1 suggest a temperature about 600-700K below the actual one while the levels of v=2 (except J=0, 1) indicate a temperature about 200-300K above the actual one (panel f). These slopes reach closer to the LTE lines, indicating the more accurate temperature, with increasing densities. Therefore, these levels could be considered as a rough temperature indicator even at low densities, and the accuracy depends on the density. The surprising result is that the populations do not appear strongly non-thermal when the molecule is far from LTE.

To see how general this quasi-thermal behavior might be, we ran additional simulations at slightly lower and slightly higher kinetic temperatures (T=1500 and 2500K). Figure 3.5 gives level population diagrams for v=1, 2 at T=1500K and T=2500K. This is for both atomic and molecular cases at a density of 10^2 cm^{-3}. The level populations are not strongly non-thermal, and the fitted slopes (not including v=2, J=0, 1) are a bit smaller than the true temperature. There is no "smoking gun" indicating that the levels are far from LTE.

The level populations will reach LTE when the density is high enough. However, from Fig. 3.4 the levels can show a quasi-thermal behavior at very low densities. This quasi-thermal behavior means that it would be easy to conclude that the gas has high density because the level populations appear to be nearly in LTE.

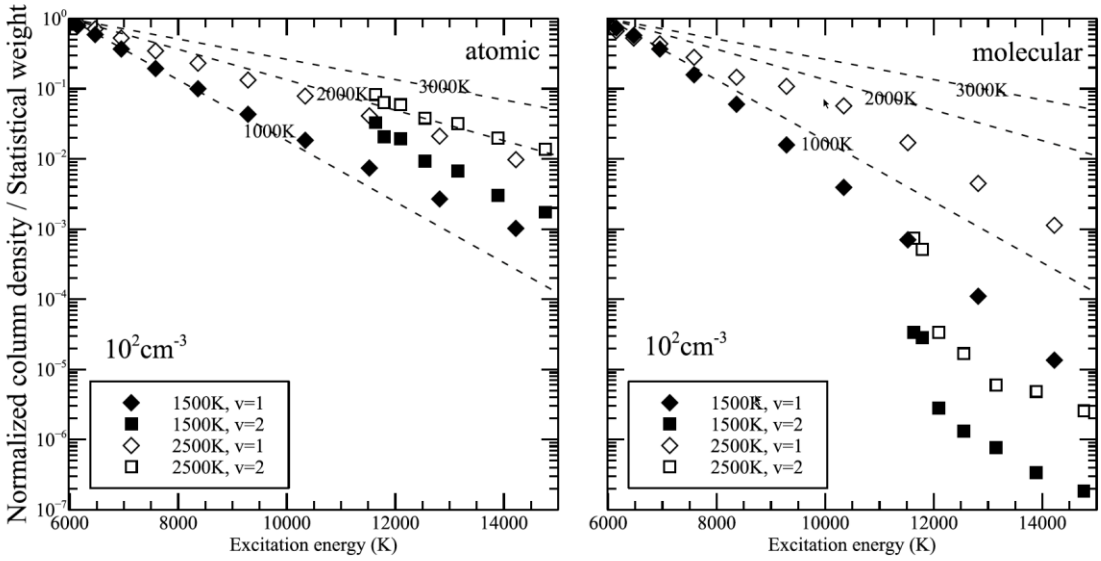

Figure 3.5 Level population diagrams for v=1, 2 within 15 000K of ground for the atomic (left) and molecular (right) cases at a gas kinetic temperature of T=1500K and T=2500K at the density of 10^2 cm^{-3}. The LTE lines are shown in dashed lines as reference.

3.5 LTE departure coefficients and mass estimates using the H_2 1-0 S(1) line

The molecule is in LTE when all populations are given by Boltzmann statistics. The density of the upper level of the line is $n_u = \left(n_{\mathrm{H_2}} g_u / Z\right) exp(-\chi/kT)$, where $n_{\mathrm{H_2}}$ is $\mathrm{H_2}$ density and Z is the partition function. The departure coefficient of a level v, J is defined as

$$b_n \equiv \frac{n_u}{n_{uLTE}} \tag{3.4}$$

where n_{uLTE} is the density of the level in LTE. The LTE critical density is the density where b_n is unity. This occurs when all populations lie along the thermal line in Fig. 3.4.

The molecular hydrogen mass M can be measured from the luminosity L of a line, the H_2 1-0 S(1) line for example, if the level population, relative to the total density of the molecule, is given by a Boltzmann function (the level is in LTE). We have

$$M = \frac{n_{\mathrm{H_2}}}{n_u} \frac{\mu}{A_{ul} h \nu_{ul}} L \tag{3.5}$$

where μ is the mass per hydrogen molecule. The departure coefficient can be seen as the amount by which the assumption of LTE causes the mass to be underestimated. We substitute Equation (3.5) into Equation (3.4) and obtain

$$M = \frac{1}{b_n} \frac{n_{\mathrm{H_2}}}{n_{uLTE}} \frac{\mu}{A_{ul} h \nu_{ul}} L \tag{3.6}$$

$$= \frac{Z}{g_u} e^{\chi/kT} \frac{\mu}{A_{ul} h \nu_{ul}} L. \tag{3.7}$$

As Fig. 3.4 shows, there are no obvious signs that the molecule is not in LTE in the atomic case when only vibrationally excited levels are detected. Such spectra could easily be mistaken as being produced by a molecule in LTE at the excitation temperature indicated.

Figure 3.6 shows the departure coefficient for the upper level of the H_2 1-0 S(1) line for different temperatures and densities. The figure shows that at moderate densities the mass can be underestimated by very large amounts.

Figure 3.7 shows the density required for the H_2 1-0 S(1) line to be within a factor of two of its LTE value. The LTE critical densities shown here are lower than suggested in Fig. 3.4 because this plot only requires that b_n be within a factor two of unity. Significantly higher densities are needed for a molecular gas due to the slower collisional rate coefficients. Densities below those shown in Fig. 3.7 will lead to more than a factor of two errors in the mass estimate. Fig. 3.3 suggests that the plasma critical density for the upper level of the H_2 1-0 S(1) line is between 10^4 cm^{-3} and 10^5 cm^{-3} for the molecular case, while Fig. 3.7 gives nearly 10^8 cm^{-3} as the minimum density to satisfy $b_n \geq 0.5$. For the atomic case the two densities are more

similar. This big difference again shows that the plasma critical density defined by Equation (3.2) is not the essential parameter for the gas to be in LTE.

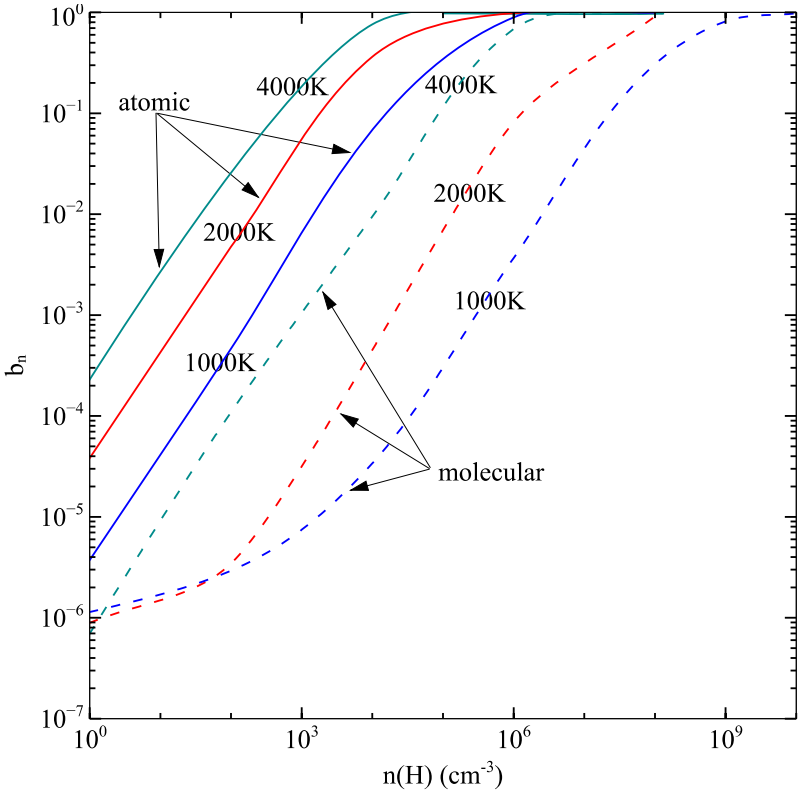

Figure 3.6 Departure coefficients b_n for the upper level of the H_2 1-0 S(1) line for different densities, atomic and molecular cases, and kinetic temperatures of T=1000K, 2000K and 4000K.

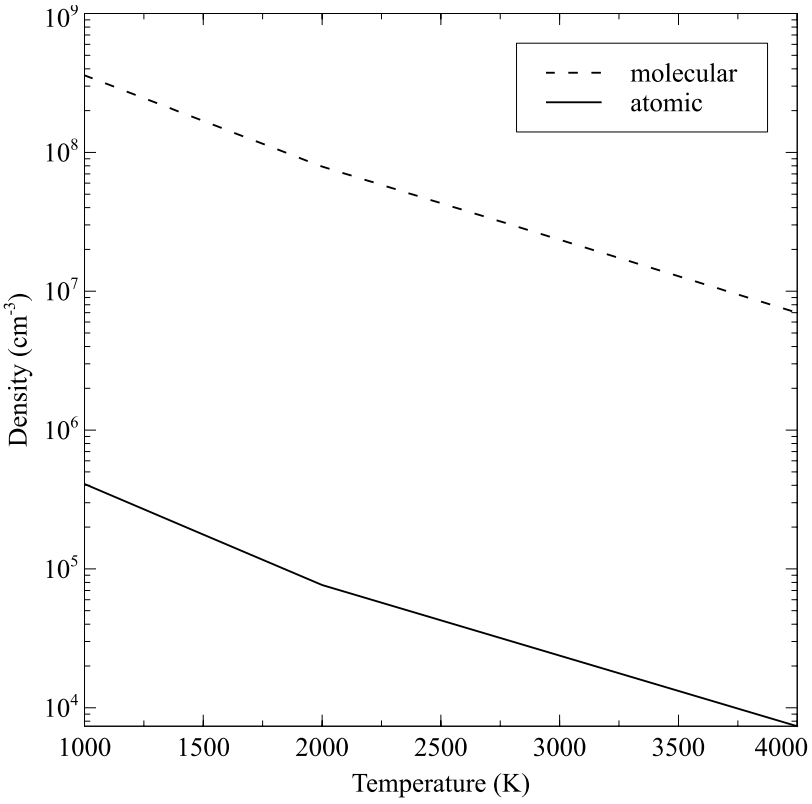

Figure 3.7 Minimum gas density required to achieve a departure coefficient $b_n \geq 0.5$ for the H_2 1-0 S(1) line as a function of temperature.

3.6 Comparison with observations

Plots such as those in Fig. 3.4 are useful if lines from levels with a broad range in excitation potentials are observed. This is easiest with space-based data, since lines from the lowest levels occur at mid-IR wavelengths. With ground-based data we are largely limited to lines within the 1-2 μm windows, which mainly come from the v=1, 2 manifolds. In this section we reconsider observations of a filament in a cool-core galaxy cluster and of the Crab Nebula, using our H_2 models.

Can we determine the density, temperature, and whether the gas is atomic or molecular, by carefully fitting and the observations with the calculations? We apply the optimization method implemented in Cloudy to deduce the gas kinetic temperature that comes closest to matching the observations for a range of assumed

densities and the two cases. We ran two grids of calculations that stepped through a series of specified gas densities in the limits that the gas was either dominated by atomic or mostly molecular collisions. For each gas density, the optimizer was then used to adjust the gas kinetic temperature to try to match the observed intensities. The results of the calculation were a deduced gas kinetic temperature and a χ^2(the goodness of fit between models and observations) value, as a function of density.

The error bars on the observations are small in many cases. However, the collisional calculations have their own errors that are introduced by uncertainties in the H^0 and H_2 collisional rates. Accordingly, we used a minimum uncertainty of 40% for atomic case and 20% for molecular case for each observed line used in the calculation, to account for the uncertainties in the interaction potentials and collision calculations (private communication with David Flower).

The two calculations presented next result in $\chi^2 < 1$ which is improbable. This may be due to a too-pessimistic estimate of the uncertainties in the collision rates. This does not affect our use of this method since we only wish to determine the density where χ^2 no longer decreases. The fits at that point are acceptable.

3.6.1 Cool-core cluster

Oonk et al. (2010) present high S/N observations of cool-core cluster filaments in Abell 2597. Table 3.1 gives their intensities and includes the error bars given in the original paper.

Oonk et al. (2010) concluded that the molecular gas is well described by a gas in LTE with a single excitation temperature of 2300K, with a density near an assumed critical density of 10^6 cm^{-3}, and dominated by collisional excitation. Jaffe et al. (2001), Edge et al. (2002), and Wilman et al. (2002) reach similar conclusions for other clusters. The resulting gas pressure is surprisingly high. For instance, for Abell 2597, this implies $nT \geq 2 \times 10^9 cm^{-3}$ K while X-ray observations find $nT \sim 3 \times$

10^6 cm^{-3} K (Tremblay et al. 2012a). One might expect the hot and cold gas to have similar pressures, and be in pressure equilibrium.

Figure 3.8 shows our predicted level populations for the levels measured by Oonk et al. (2010). Both the atomic and molecular cases with different hydrogen densities are shown. Fig. 3.8(f) shows the observed populations with their uncertainties. The error bars for most lines are too small to be seen relative to the size of the plot symbols. The downward arrows in the prediction panels indicate levels whose populations are so small that they are off the bottom of the scale.

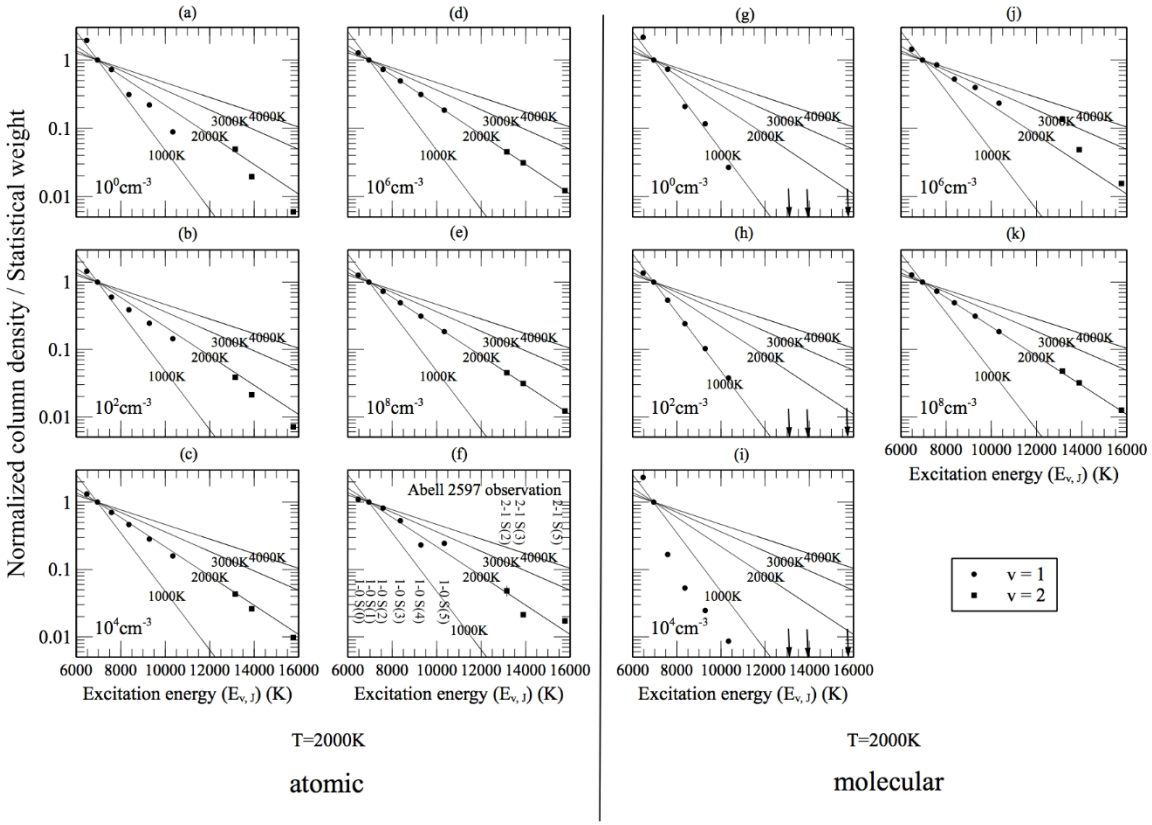

Figure 3.8 Panel (f) shows the observations of the cool-core cluster Abell 2597. Other panels show the predicted levels in the same way as the observed levels in (f), for both the atomic and molecular cases for different hydrogen densities at T=2000K.

Figure 3.9 shows the optimization results, with the atomic case on the left and the molecular case on the right. (The Crab Nebula, discussed next, is also shown.) The upper panel shows the best-fitting gas kinetic temperature for the atomic and molecular cases. As suggested by Figs. 3.4, 3.8 and 3.9 and by Le Bourlot et al. (1999), the derived temperature decreases slightly as the density increases for the atomic case, since the populations are not completely thermal (Figs. 3.8 and 3.9). This is not true for the molecular case. The lower two panels give the χ^2 goodness of fit. These use 1 sigma uncertainties that include the uncertainty in the collision rates described above. We find for the atomic case χ^2 decreases quickly with increasing gas density. There are no good solutions for the molecular case, but high densities help.

The χ^2 values can constrain the physical conditions. We find χ^2 to be small at intermediate and high densities for the atomic case but relatively large for much of the density range for the molecular case. For the atomic case any density greater than 10^2 cm^{-3} is allowed and the temperature is constrained to be about 2000-2200K. This density limit includes the density derived by the original study but allows values 4 dex below it. There is no upper limit to the allowed density since the levels have gone into LTE. For the molecular case the density must be very high, about 10^8 cm^{-3}, with the temperature again about 2000K, but the χ^2 is about five times larger than for the atomic case. This density is 2 dex higher than the value derived in the original paper.

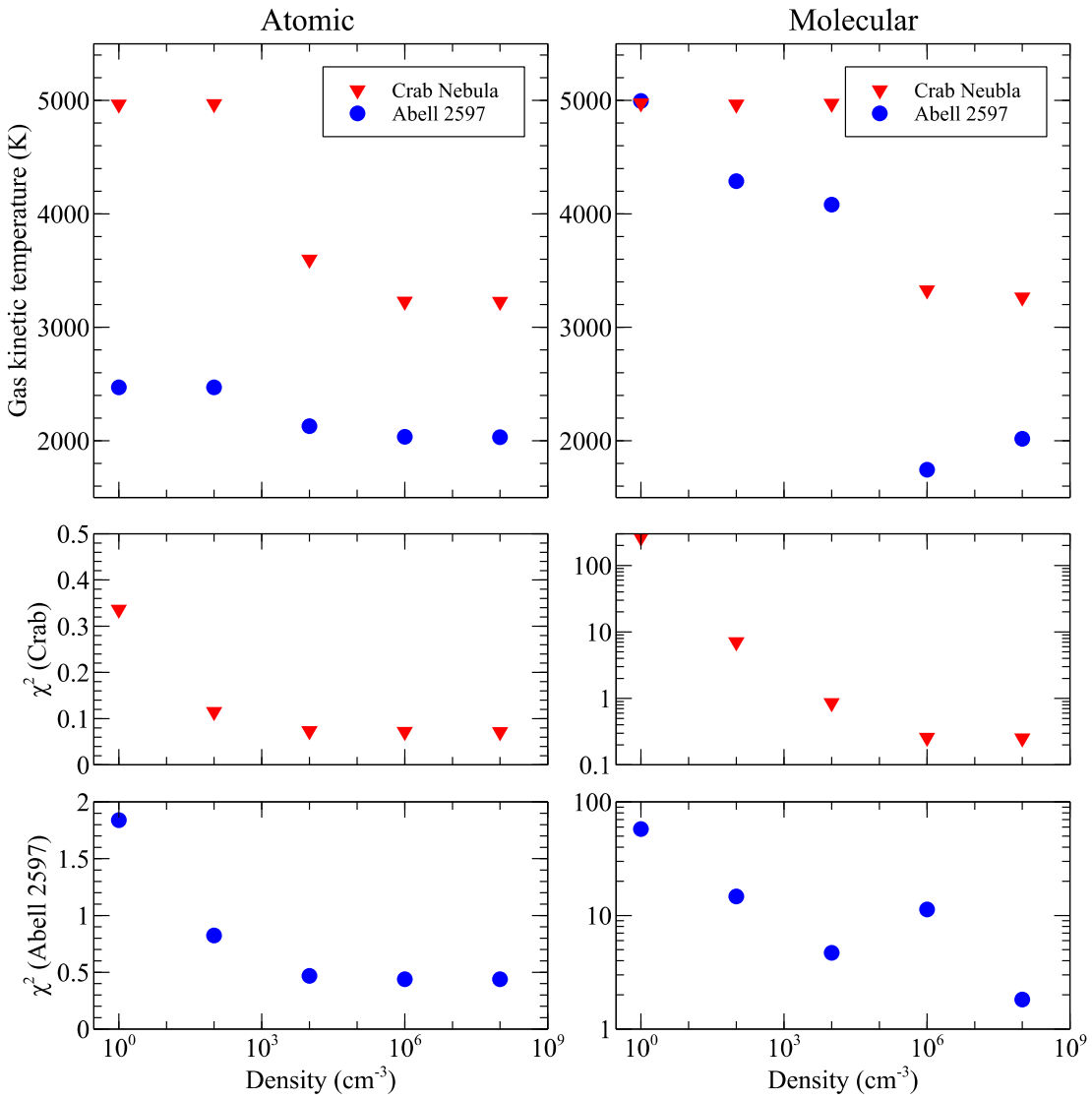

Figure 3.9 Optimized temperatures and the corresponding reduced χ^2 values as a function of density for Knot 1 of the Crab Nebula and for Abell 2597, for both the atomic and molecular cases.

These derived density and temperature can be used to determine the pressure in the H_2-emitting gas. For the atomic case we have good fits with $nT \geq 2 \times 10^5$ cm^{-3} K while for the molecular case we have a poor fit with $nT \geq 2 \times 10^{10}$ cm^{-3} K. Oonk et al. (2010) find n $\geq 2 \times 10^9$ cm^{-3} K for the warm gas that emits NIR H_2 lines, but $nT \sim 2 \times 10^6$ cm^{-3} K for the warm ionized gas that produces optical H I recombination lines. This pressure imbalance between the molecular gas

and the ionized gas has been previously noted by Jaffe et al. (2005). For comparison, the pressure inferred for the surrounding X-ray emitting hot ionized gas is $nT \sim 5 \times 10^6$ cm^{-3} K (Tremblay et al. 2012a), which is roughly consistent with the warm ionized gas pressure.

Our analysis shows that the density of the gas emitting the NIR H_2 lines can be substantially below that needed for LTE. The atomic case is both a better fit and results in pressures consistent with the surrounding hot gas. If the H_2-emitting gas has a density of $n \sim 2.5 \times 10^3$ cm^{-3}then it is in pressure equilibrium with both the warm ionized and hot ionized gas. We assume constant pressure, adopt this density, and assume that the atomic case holds. We shall refer to the NIR H_2-emitting gas as the "warm atomic" phase in the following discussion.

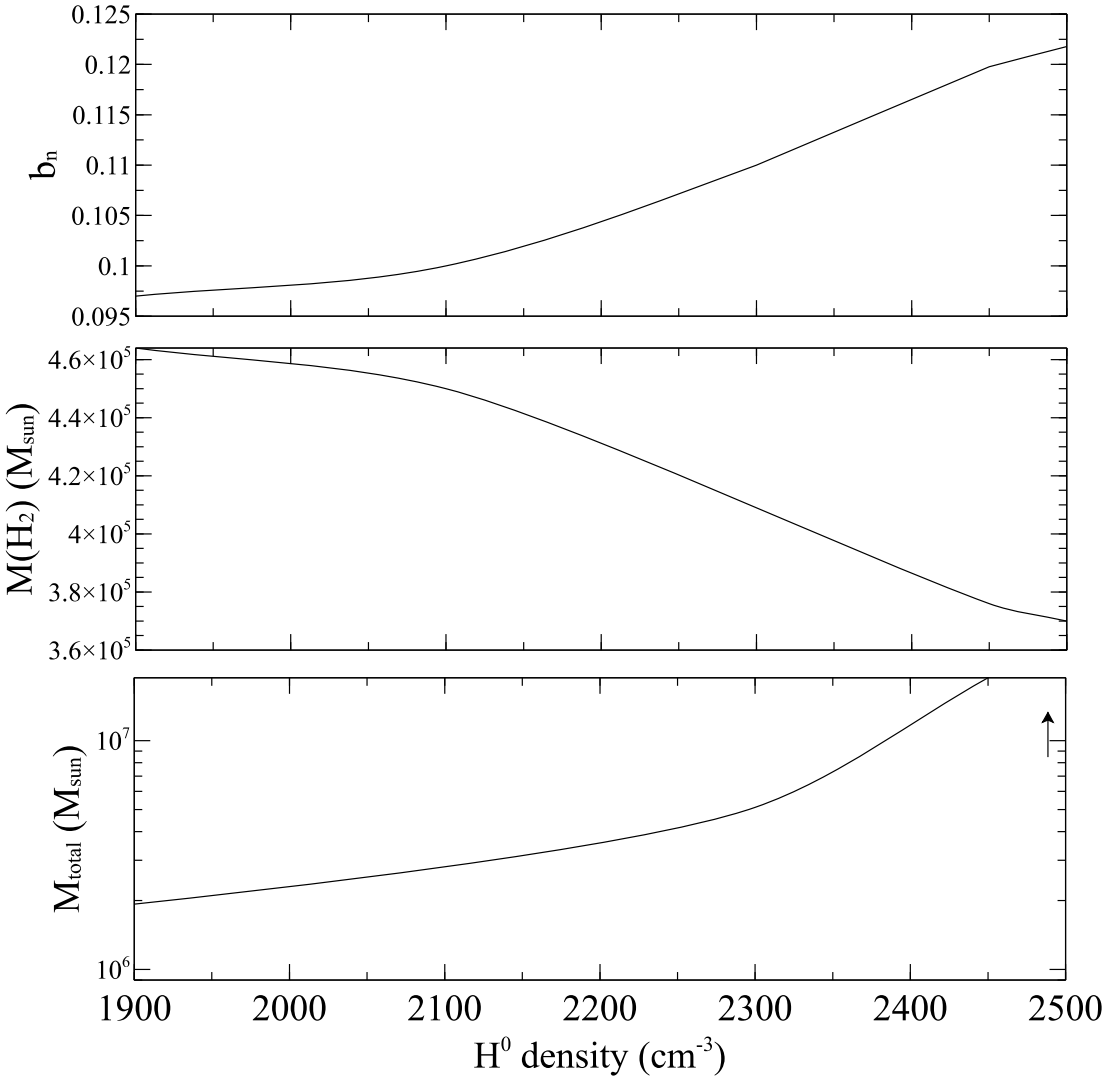

Figure 3.10 The departure coefficient, corrected H_2 mass and the total mass (H^0 and H_2) as a function of the H^0 density in Abell 2597. A temperature of 2000 K and the hot gas pressure was assumed.

Figure 3.10 and Table 3.2 summarize estimates of the total mass of the warm atomic phase. We find that H^0 collisions dominate the level populations in the warm atomic phase and that the hydrogen density must be greater than 100 cm^{-3}. The examples computed above show that atomic collisions will dominate if $n(H^0)/n(H_2) > 3$. This, and a temperature selection effect, are described further below. The H_2 mass in the warm atomic phase can be estimated from the H_2 1-0 S(1) line after taking its sub-

thermal population into account. Oonk et al. (2010) find a warm H_2 mass of $M(H_2) \sim 4.5 \times 10^4 M_{sun}$ assuming LTE. The correction for sub-thermal populations (Fig. 3.4 and the top panel of Fig. 3.10) raises the H_2 mass by a factor of $1/b_n$ calculated from Fig. 3.6. This gives the H_2 mass indicated in Fig. 3.10 and Table 3.2, which depends on the H^0 density but is about an order of magnitude higher than the LTE value. Current observations do not allow the direct measurement of H^0 and the modeling does not depend on the ratio as long as $n(H^0)/n(H_2) > 3$, so we really have only a lower bound to $M(H^0)/M(H_2)$, $M(H^0)/M(H_2) = n(H^0)/2n(H_2) > 1.5$.

If we assume that the warm atomic phase is in pressure equilibrium with the surrounding hot gas then we can estimate the total mass. Taking the pressure inferred for the surrounding X-ray emitting hot ionized gas (Tremblay et al. 2012a) and our measured kinetic temperature of 2000K, then the range of the densities of H^0 and H_2 is restricted by the equation $[n(H^0)+2n(H_2)]\times 2000K = 5\times 10^6$ cm^{-3} K where $n(H^0)+2n(H_2) \sim 2.5 \times 10^3$ cm^{-3}. Table 3.2 and Fig. 3.10 take the H^0 density as a free parameter over the range 1900 cm^{-3} (the lowest density for the H^0 to dominate the collisions since $n(H^0)/n(H_2) > 3$ (section 2.2)) to 2500 cm^{-3} (the density where H^0 alone accounts for the full gas pressure). Column 1 gives this density and column 2 gives the required H_2 density. Table 3.2 also gives the derived atomic, molecular, and total mass. Fig. 3.10 shows the results given by Table 3.2 as a function of the H^0 density. The upper panel shows the departure coefficient b_n calculated from the atomic case at T=2000K in Fig. 3.6. The middle panel gives the H_2 mass corrected for sub-thermal populations. The lower panel shows M_{total}, the total mass of the H^0 and H_2 which is considered as the mass of the warm atomic phase. The highest H^0 density case corresponds to essentially no H_2 so the total mass is only a lower limit. The arrow in the lower panel indicates that the mass would be extremely large when the gas includes only H^0.

This is only the mass in the spectroscopically active warm atomic gas, gas warm enough to emit in the NIR. Other gas phases, summarized in Table 3.3, are present in Abell 2597. Extensive reservoirs of cold gas, T<10^3 K could only be seen in heavy-

element molecular emission such as CO. Tremblay et al. (2012b) detect this gas and find its mass is $\sim 1.8 \pm 0.3 \times 10^9 M_{sun}$. As Ferland et al. (2009) note, very cold, T<10^2 K, gas should also exist, but could not be detected with current observations.

3.6.2 Crab Nebula

Loh et al. (2012) used K-band spectra to measure the H_2 excitation temperatures in Knot 1 of the Crab Nebula. They find that the H_2 lines could be fitted by LTE populations at a temperature of about 3200K, based primarily on the ratio of the 2-1 S(1) and 1-0 S(1) lines, with a density of roughly 10^4 cm^{-3}. Figure 3.11 compares the predicted and observed level populations. The downward arrow in Fig. 3.11(f) gives the observed upper limit. The deduced excitation temperature is high in the Crab filament, roughly 3000 K (Loh et al. 2012), so we computed models at this temperature.

Results for optimized models are shown in Fig. 3.9. We find χ^2 to have reached a minimum value for $n \geq 10^2$ cm^{-3} for the atomic case and $n \geq 10^4$ cm^{-3} for the molecular case. For both cases the derived temperatures are around 3300K. The χ^2 is roughly 3 times lower for the atomic case than for the molecular case.

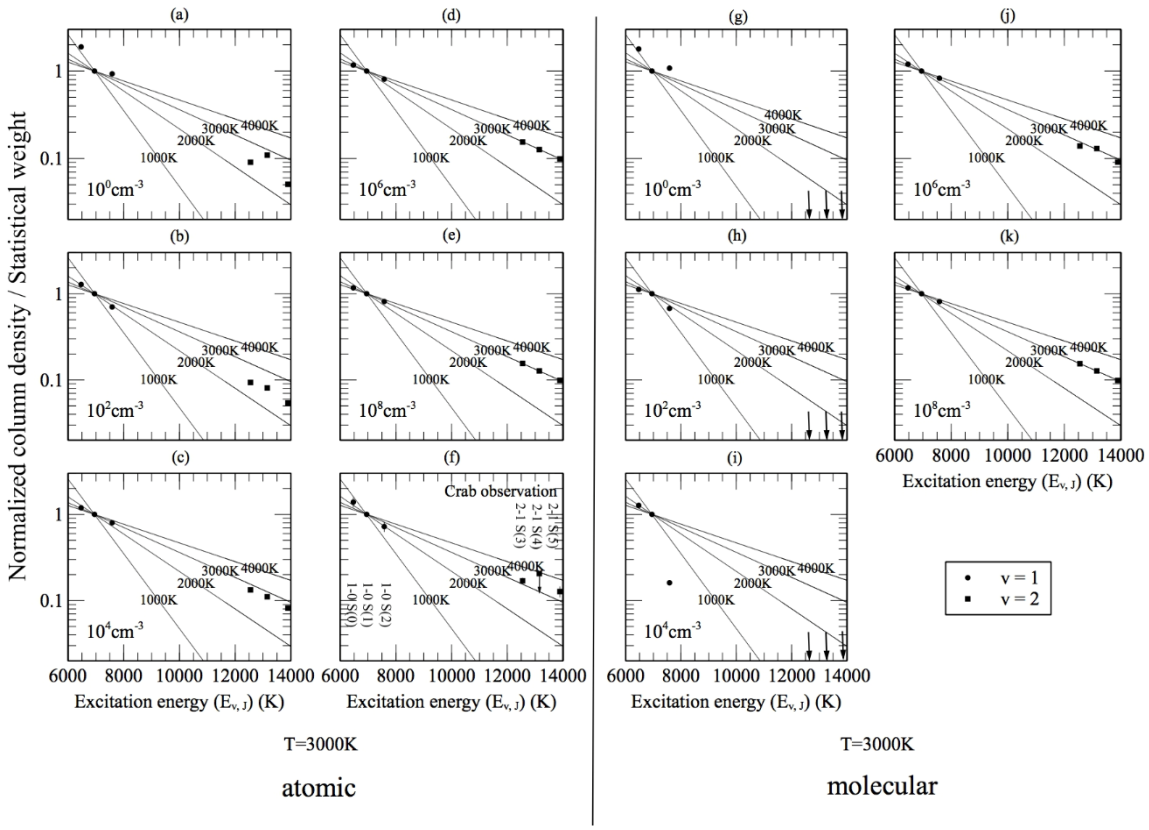

Figure 3.11 Panel (f) shows observations of Knot 1 of the Crab nebula. Other plots show the predicted levels for both atomic case and molecular cases, for different hydrogen densities, and a temperature of 3000K which was chosen to be close to the observed value.

These results are consistent with both the density and temperature deduced by Richardson et al. (2013), who found that the core of Knot 51 is dominated by the atomic collisions. However, our optimization of the Knot 1 observations cannot rule out the molecular case. The pressures for both cases, $nT \geq 5 \times 10^5$ cm^{-3} K for the atomic case and $nT \geq 4.8 \times 10^7$ cm^{-3} K for the molecular case, are roughly consistent with that derived from the H$^+$ gas using the [S II] lines, $nT \sim 4.5 \times 10^7$cm^{-3} K (Loh et al. 2012).

For the atomic case, if the density of 10^2 cm^{-3} is allowed, the corresponding temperature is about 5000K and the departure coefficient $b_n \approx 0.04$ (although we do not show the calculations for 5000K in Fig. 3.6). Therefore, the H_2 mass will be 25

times larger than the mass when the LTE assumption holds. For the molecular case, $b_n \approx 0.34$ when the density is 10^2 cm^{-3} at T=5000K, which results in a factor of 3 error for the mass

Table 3.1 Relative line intensities of Abell 2597 and Crab Nebula

Transition	Wavelength (μm)	Relative Intensity (Abell 2597)[1]	Relative Intensity (Crab)[2]
H_2 1-0 S(2)	2.0338	0.419±0.013	0.37±0.05
H_2 2-1 S(3)	2.0735	0.057±0.003	0.34±0.05
H_2 1-0 S(1)	2.1218	1.000±0.022	1±0.03
H_2 2-1 S(2)	2.1542	0.033±0.006	<0.14
H_2 1-0 S(0)	2.2235	0.182±0.017	0.23±0.03
H_2 2-1 S(1)	2.2477	-	0.23±0.02
H_2 1-0 S(3)	1.9576	1.094±0.029	-
H_2 1-0 S(4)	1.8920	0.194±0.011	-
H_2 1-0 S(5)	1.8358	0.691±0.017	-
H_2 2-1 S(5)	1.9449	0.059±0.006	-

[1, 2] Both are relative line intensity. The reference line is H_2 1-0 S(1) 2.1218 μm.

Table 3.2 The mass of the H_2 emitting phase in Abell 2597

$n(H^0)$ (cm^{-3})	$n(H_2)$ (cm^{-3})	b_n	$M(H_2)$ (M_{sun})	$M(H^0)$ (M_{sun})	M_{total} (M_{sun})
1900	300	0.097	4.64×10^5	1.47×10^5	1.93×10^6
2100	200	0.1	4.5×10^5	2.36×10^6	2.81×10^6
2300	100	0.11	4.09×10^5	4.7×10^6	5.11×10^6
2500	0	0.12	3.46×10^5	$> 10^8$	$> 10^8$

Table 3.3 Properties of different gas phases in Abell 2597

Phase	Tracer	Hydrogen Density (cm^{-3})	Temperature (K)	Pressure (cm^{-3} K)	Mass (M_{sun})	Reference
Hot ionized	X-ray	~ 0.1	$\sim 3 \times 10^7$	$\sim 5 \times 10^6$	-	Tremblay et al. (2012b)
Warm ionized	H I optical	~ 200	$\sim 10^4$	$\sim 2 \times 10^6$	$\sim 10^7$	Oonk et al. (2010)
Warm atomic	H_2 NIR	$\sim 2.5 \times 10^3$	~ 2000	$\sim 5 \times 10^6$	$\geq 1.93 \times 10^6$	This paper
Cold molecular	CO	$\sim 5 \times 10^4$	~ 100	$\sim 5 \times 10^6$	$\sim 1.8 \times 10^9$	Tremblay et al. (2012b)
Very cold molecular	None	$> 5 \times 10^4$	<100	$\sim 5 \times 10^6$	Unknown	Ferland et al. (2009)
Total mass					$> 2 \times 10^9$	

3.7 Conclusions

This paper was motivated by observations showing the near infrared H_2 lines to be much stronger than neighboring H I recombination lines in spectra of Helix knots, filaments in the Crab Nebula, and filaments in cool-core clusters. Many subtle processes like grain formation or photo pumping can excite H_2, but the H_2 emission produced by such processes is quite weak. Our detailed modeling (Henney et al. 2007, Ferland et al. 2009, Richardson et al. 2013) has shown that strong H_2 lines in these environments are produced by thermal collisions. Temperatures are near 2000 K due to powerful selection effects. In order to gain a better understanding of what information is actually contained in H_2 emission and the derived level population diagrams, we have investigated the simplified case where H_2 is only excited by thermal collisions. We have calculated H_2 level populations for thermal collisional excitation in two limits, the first dominated by atomic collisions, and the second dominated by molecular collisions. We show these populations for various densities with the goal of quantifying how H_2 emission can be used to probe

conditions in an otherwise unknown medium. Can the H_2 populations be used to determine the physical state of the gas (atomic or molecular), its temperature, and the density?

The key message of Figs. 3.8 and 3.11 is that nearly all densities for the atomic gas, and some densities for the molecular cases, could be fitted using a single excitation temperature. Only a few points deviate from such a single excitation temperature to varying degrees. These apparently wild points could be misinterpreted as due to unrecognized calibration errors or noise sources in the observations, and mistakenly be ignored. The excitation temperatures are generally smaller than the gas kinetic temperature except at the highest density, where the levels have gone to LTE. This again points out how easy it is to misunderstand what these level population diagrams are telling us. The result is that the observations do not strongly constrain the density.

We reach the following conclusions, many of which were implicit in previous calculations. We focus on the level population diagrams, and compare the actual populations with what they would be in LTE, where the populations are given by Boltzmann factors.

- The deviations from LTE depend on density and whether the collision is predominantly atomic or molecular. At a given particle density, the H_2 level populations will be much closer to LTE for the atomic case than for the molecular case due to the larger collision rates.

- These deviations from LTE tend to mimic those produced by either fluorescence (Draine & Bertoldi 1996) or shocks (Flower et al. 2010), so it is important to be cautious when making such interpretations.

- The collisional coupling between levels in a single vibrational manifold is larger than the rates between different manifolds. This means that the relative level populations within a single manifold will approach a quasi-Boltzmann distribution at lower densities than population ratios involving different manifolds. This means that H_2 population ratios involving one manifold will be a valid temperature indicator at lower densities than ratios involving different manifolds. The distortion away from a Boltzmann distribution at lower densities changes the slope of the level population diagram for levels causing the populations to indicate an excitation temperature that is lower than the kinetic temperature. The v=0 manifold is the worst case.

- Near T=2000K, even at very low densities, the v=1, 2 level populations roughly fall on a straight line for both the atomic and molecular cases. The populations are sub-thermal at low densities so the kinetic temperature will be underestimated. Without observations of v=0 levels, it would be easy to conclude that the gas has high density because the level populations appear to be nearly in LTE.

- At low densities for the molecular case, the v=0 and v=1 vibrational manifolds do not join into each other smoothly. The v=2, J=0, 1 and the other higher J levels in the same vibrational manifold are also discontinuous. These separations are different for different densities as well as different excitation energies. These discontinuous behaviors could be used as both a density and molecular region diagnostic.

- Comparing the calculations of pure collisional models with some other H_2 excitation models shown in Fig. 3.1, we find that the PDR models produce level population diagrams that are similar to the atomic case. We examined these predictions in detail and find that the levels are indeed mainly excited

in atomic gas. The C-shock calculation populations are very similar to the molecular case and the lines do arise in molecular regions. The J-shock calculation is quite similar to the atomic case, but we find that different levels are populated in different regions. Higher vibrational excited levels are populated mainly in warmer atomic gas while the low-lying rotational levels are produced in cool molecular gas. This shows the utility of the diagnostics given in this paper.

- We did a χ^2 best fit of our NLTE predictions to H_2 observations. For the cool-core cluster Abell 2597, the preferred models are predominantly atomic with $n(\mathrm{H}) \geq 10^2$ cm^{-3} and T~2000 K. This minimum required density is much smaller than the LTE density of 10^6 cm^{-3} that was derived in earlier studies. The gas pressure is consistent with the pressure in the surrounding X-ray gas if the density is $n(\mathrm{H}) = 2.5 \times 10^3$ cm^{-3}. The density is overestimated and the total mass is underestimated when only H_2 in LTE is considered. We find that the total mass of the warm gas producing the NIR H_2 emission is $M \geq 1.93 \times 10^6 M_{sun}$ and it could be as high as > $10^8\ M_{sun}$. For comparison the mass of the cold molecular gas of $\sim 1.8 \pm 0.3 \times 10^9 M_{sun}$ was found by Tremblay et al. (2012b). It is likely that undetectable reservoirs of very cold gas are also present.

- For the χ^2 fitting to H_2 in the Crab Nebula, we find that $n(\mathrm{H}) \geq 10^2$ cm^{-3} for the atomic case and $n(\mathrm{H}) \geq 10^4$ cm^{-3} for the molecular case are required. Both fits are acceptable. The gas pressure derived for both the atomic and molecular cases is roughly consistent with the pressure previously determined for the adjacent H^+ region by using the [S II] lines.

- Determining the density, and whether the gas is dominated by atomic or molecular collisions, from H_2 observations is possible if a broad range of

levels can be observed. Far-infrared measurements of v=0 lines and their comparison to the v=1, 2 manifold offers the best hope.

- The LTE critical density is that needed for populations to be thermal. The population of the level producing the familiar H_2 1-0 S(1) line goes to LTE at relatively high densities, much higher than the densities needed to have the relative populations within a manifold appear thermal. The mass in H_2 would be underestimated, sometimes by large factors, if LTE were assumed to convert a line luminosity into a mass.

CHAPTER 4 Conclusions

This work explores the physics of a possible unseen outer shell surrounding the visible Crab Nebula. This is suggested by the Crab's relatively low mass and kinetic energy. The molecular hydrogen emission due to a simple hydrogen-only model can be used as both density and temperature indicators by investigating the level population diagrams. The results of this work can be applied to future study on both the supernovae remnants and the interstellar medium. The conclusions of this work are summarized below.

In Chapter 2, different photoionization models have been studied on the outer shell of the visible Crab Nebula. The following points are the major conclusions: Compared to the age of the Crab Nebula, the gas cooling time is much longer. As a result, the unseen outer shell is not in thermal equilibrium. The unseen outer shell is in ionization equilibrium because the age of the Crab Nebula is much longer than the recombination time scale. Thus, the unseen outer shell must be highly ionized but the temperature is uncertain. The infrared coronal lines in our models are very strong, much stronger than most of the optical emissions, which indicates that the infrared lines are the best hope to find such an outer shell. Observers should focus on searching for these strong infrared lines other than the fainter optical lines for the unseen outer shell. A C IV absorption feature can be produced if line broadening is small in the line-forming regions. To obtain the reliable prediction of the C IV optical depth, fully dynamical models are needed. Models with $\alpha < -4$ probably could be excluded because the observational limit is below the surface brightness of the models for $\alpha = -4$ for both ISM and solar abundances.

In Chapter 3, the properties of the simple pure hydrogen gas excited only by collisions have been studied. The H_2 level populations diagrams have been explored as a major tool to derive the temperature and density. Several conclusions are obtained as below. The level populations of the H_2 would be closer to the LTE at a given density for the atomic case than the molecular case because collisional rates

for the molecular case are much smaller. The level populations within a single vibrational manifold can approach a quasi-thermal distribution even at very low densities, much lower than the densities required for the gas to be in LTE. This means that the level populations within one vibrational manifold could be considered as a valid gas temperature when the populations involved in different vibrational manifolds cannot. At the temperature of 2000 K, the level populations for $v = 1$ and 2 are roughly parallel to the LTE line even at very low densities for both atomic and molecular cases. The populations would be sub-thermal at low densities so the gas kinetic temperature would be underestimated. Without the observations of $v = 0$, it would be easy to misinterpret the populations as being close to LTE. For the molecular case, a density indicator can be obtained by using the separations between the $v = 0$ and 1 vibrational manifold populations, as well as the discontinuous behavior between $v = 2$, J=0, 1 and the other higher J levels in the same vibrational manifolds. The level population diagrams produced by the PDR models are similar to the atomic case. The calculated level populations of the C-shock models are similar to the molecular case while the J-shock populations are similar to the atomic case. The optimization results obtained from CLOUDY calculations show that mass of the Abell 2597 can be largely underestimated while the result for the Crab Nebula are roughly consistent with the previous publications. The LTE critical density for levels to be thermal is very high, much higher than the densities needed to have the relative populations within a manifold to be thermal. The mass of the H_2 could be underestimated largely if the LTE were assumed to convert a line luminosity into a mass.

Bibliography

Badnell, N. R., 2006, ApJS, 167, 334
Badnell, N. R., O'Mullane, M. G., Summers, H. P., Altun, Z., Bautista, M. A., Colgan, J., Gorczyca, T. W., Mitnik, D. M., Pindzola, M. S., Zatsarinny, O., 2003, A&A, 406, 1151
Bietenholz, M. F. & Kronberg, P. P. 1990, ApJL, 357, L13
Black, J. H. & van Dishoeck, E. F., 1987, ApJ, 322, 412
Carroll, B. W. & Ostlie, D. A. 2006, An Introduction to Modern Astrophysics (2nd ed.; San Francisco, CA: Addison-Wesley)
Chevalier, R. A., 1977, in Schramm, D., ed., Astrophysics and Space Science Library, Vol. 66, Supernovae. Springer, Berlin, p. 53
Clark D. H., et al., 1983, MNRAS, 204, 415
Comella, J.M., Craft, H. D., Lovelace, R. V. E., & Sutton, J. M. 1969, Natur, 221, 453
Davidson, K., Fesen, R.A., 1985, ARA&A, 23, 199
Draine, B. T., 2011, Physics of the interstellar medium and intergalactic medium. Princeton Univ. Press, Princeton, NJ
Draine, B. T., & Bertoldi, Frank, 1996, ApJ, 468, 269
Edge, A. C., Wilman, R. J., Johnstone, R. M., Crawford, C. S., Fabian, A. C., Allen, S. W., 2002, MNRAS, 337, 49
Ferland, G. J., 1980, PASP, 92, 596
Ferland, G. J. 2011, Proceedings of the conference, Narrow-Line Seyfert 1 Galaxies and their place in the Universe, ed. Luigi Foschini (chair), Monica Colpi, Luigi Gallo, Dirk Grupe, Stefanie Komossa, Karen Leighly, Smita Mathur (Milano, Italy), 13
Ferland, G. J., Fabian, A. C., Hatch, N. A., Johnstone, R. M., Porter, R. L., van Hoof, P. A. M., Williams, R. J. R., 2008, MNRAS, 368, L72
Ferland, G. J., Fabian, A. C., Hatch, N. A., Johnstone, R. M., Porter, R. L., van Hoof, P. A. M., & Williams, R. J. R., 2009, MNRAS, 392, 1475
Ferland, G. J., Porter, R. L., van Hoof, P. A. M., Williams, R. J. R., Abel, N. P., Lykins, M. L., Shaw, Gargi, Henney, W. J., Stancil, P. C., 2013, RMxAA, 49, 137
Fesen, R. A., Shull, J. M., Hurford, A. P., 1997, AJ, 113, 354
Fillippenko A. V., 1997, ARA&A, 35, 309
Flower, D. R.; Pineau Des Forêts, G., 2010, MNRAS, 406, 1745
Gaensler B. M. & Slane P. O., 2006, ARA&A, 44, 17
Graham, J. R., Wright, G. S., & Longmore, A. J., 1990, ApJ, 352, 172
Henney, W. J., Arthur, S. J., Williams, R. J. R., Ferland, G. J., 2005, ApJ, 621, 328
Henney, W. J., Williams, R. J. R., Ferland, G. J., Shaw, G., O'Dell, C. R., 2007, ApJ, 671, 137
Hester, J. J., 2008, ARA&A, 46, 127
Hester J. J. et al., 2002, ApJ, 577, L49
Jaffe, W., Bremer, M. N., & Baker, K. 2005, MNRAS, 360, 748
Jaffe, W., Bremer, M. N., & van der Werf, P. P. 2001, MNRAS, 324, 443
Johnstone, R. M., Hatch, N. A., Ferland, G. J., Fabian, A. C., Crawford, C. S., & Wilman, R. J., 2007, MNRAS, 382, 1246
Kitaura, F. S., Janka, H.-T., Hillebrandt W., 2006, A&A, 450, 345
Le Bourlot, J., Pineau des Forêts, G., & Flower, D. R., 1999, MNRAS, 305, 802

Le Bourlot, J., Pineau des Forêts, G., Roueff, E., Dalgarno, A., & Gredel, R., 1995, ApJ, 449, 178
Loh, E. D., Baldwin, J. A., & Ferland, G. J., 2010, ApJL, 716, L9
Loh, E. D., Baldwin, J. A., Curtis, Z. K., Ferland, G. J., O'Dell, C. R., Fabian, A. C., & Salomé, Philippe, 2011, ApJS, 194, 30
Loh, E. D., Baldwin, J. A., Ferland, G. J., et al., 2012, MNRAS, 421, 789
Loll, A. 2010, PhD thesis, Arizona State Univ.
Lundqvist, P., Fransson, C., Chevalier, R. A., 1986, A&A, 162, L6
Lundqvist, P., Tziamtzis, A., 2012, MNRAS, 423, 1571
Mitton, S., 1980, The Crab Nebula, Charles Scribner's Sons, New York
Nomoto, K., 1987, ApJ, 322, 206
Nomoto, K., 1985, in Kafatos M. C., Henry R. B. C., eds, The Crab Nebula and Related Supernova Remnants. Cambridge Univ. Press, Cambridge, p. 97
O'Dell, C. R., Henney, W. J., & Ferland, G. J., 2005, AJ, 130, 172
O'Dell, C. R., Henney, W. J., & Ferland, G. J., 2007, AJ, 133, 2343
Oonk, J. B. R., Jaffe, W., Bremer, M. N., & van Weeren, R. J., 2010, MNRAS, 405, 898
Osterbrock, D. E., Ferland, G. J., 2006, Astrophysics of Gaseous Nebulae and Active Galactic Nuclei, Univ. Science Books, Mill Valley, CA
Pequignot, D., Dennefeld, M., 1983, A&A, 120, 249
Richardson, C. T., Baldwin, J. A., Ferland, G. J., Loh, E. D., Kuehn, C. A., Fabian, A. C., Salomé, Philippe, 2013, MNRAS, 430, 1257
Riffel, R. A., Storchi-Bergmann, & Nagar, N. M., 2010, MNRAS, 404, 166
Staelin, D. H. & Reifestein, E. C. 19
Röllig, M. et al., 2007, A&A, 467, 18768, Sci, 162, 1481
Sankrit, R., Hester, J. J., 1997, ApJ, 491, 796
Sollerman, J., Lundqvist, P., Lindler, D., Chevalier, R. A., Fransson, C., Gull, T. R., Pun, C. S. J., Sonneborn, G., 2000, ApJ, 537, 861
Sternberg, A., & Dalgarno, A., 1989, ApJ, 338, 197
Sternberg, A., & Neufeld, D. A., 1999, ApJ, 516, 371
Storey, P. J., Hummer, D. G., 1995, MNRAS, 272, 41
Sun, Y., & Dalgarno, A., 1994, ApJ, 427, 1053
Shaw, G., Ferland, G. J., Abel, N. P., Stancil, P. C., & van Hoof, P. A. M., 2005, ApJ, 624,794
Takahashi, J., & Uehara, H., 2001, ApJ, 561, 843
Tielens, A. G. G. M., 2005, The physics and chemistry of the interstellar medium. Cambridge Univ. Press, Cambridge, UK
Tielens, A. G. G. M., Hollenbach, D., 1985, ApJ, 291, 722
Tremblay, G. R. et al., 2012a, MNRAS, 424, 1026
Tremblay, G. R. et al., 2012b, MNRAS, 424, 1042
van Dishoeck, E. F., 2004, ARA&A, 42, 119
Wilman, R. J., Edge, A. C., Johnstone, R. M., Fabian. A. C., Allen, S. W., Crawford. C. S., 2002, MNRAS, 337, 63
Wolniewicz, L., Simbotin, I., & Dalgarno, A., 1998, ApJS, 115, 293
Wrathmall, S. A., Gusdorf, A., & Flower, D. R., 2007, MNRAS, 382, 133

VITA

Xiang Wang

EDUCATION

Ph.D. Physics ..... expected May 2016
University of Kentucky, Lexington, Kentucky, United States

M.Sc. Physics ..... August 2013
University of Kentucky, Lexington, Kentucky, United States

B.S. Physics ..... June 2007
Sichuan Normal University, Chengdu, Sichuan, China

PROFESSIONAL POSITIONS HELD

Graduate Research Assistant ..... May 2011- present
University of Kentucky, Lexington, KY

Teaching Assistant ..... Aug 2010 - May 2011
University of Kentucky, Lexington, KY

HONORS

NSF ALMA Fellow, 2014-2015

PUBLICATIONS

Wang, Xiang, Ferland, G. J., Baldwin, J. A., Loh, E. D., Richardson, C. T., "Detecting the Rapidly Expanding Outer Shell of the Crab Nebula: Where to Look", 2013, ApJ, 774, 112

Wang, Xiang, Ferland, G. J., Baldwin, J. A., Loh E. D., Fabian, A. C., Williams, R. J. R., "Molecular Hydrogen Emission as a Density and Temperature Indicator", submitted to MNRAS

SOCIETY MEMBERSHIPS

American Physical Society
American Astronomical Society